



## Master Thesis - Supplementary Corrections -

Institute of Fluid Mechanics and Environmental Physics  
in Civil Engineering, ISU

Federal Institute for Geosciences and Natural Resources, BGR

# NUMERICAL INVESTIGATION OF TRANSIENT WATER FLOW IN THE CHTOUKA AQUIFER, MOROCCO

Starting date: **01.01.2022**

Deadline: **07.10.2022**

Submitted by: **Michael Weber**  
Studiengang: **Umweltingenieurwesen PO 2019**

First Examiner: **apl.-Prof. Dr. Thomas Graf**

Second Examiner: **Dr. Georg Houben**

Supervisor: **Dr. Nelly Montcoudiol**



# Abstract

Michael Weber

Student at Leibniz Universität Hannover  
weber@stud.uni-hannover.de

The Chtouka plain in South-Western Morocco represents an important contributor to federal agricultural production. As it is located in a region of semi-arid climate, extensive irrigation is required to sustain the cultivated plant species. Due to lack of sufficient surface water sources, water demand is met by groundwater extraction from the Chtouka aquifer. Since the midst of the 20<sup>th</sup> century groundwater overexploitation developed which led to significant drawdowns of the local groundwater table of 20 m and more in recent years. This drawdown results in intrusion of saltwater from the adjoining Atlantic Ocean into coastal areas and further depletes available freshwater resources. On administrative level, in the last two decades a number of measures have been taken to counteract this development. However, the assessment of these and future management decisions heavily relies on information about the state and response of the aquifer. For this, groundwater models have proven a valuable instrument to predict impacts of measures and future developments.

Within a preceding work by Horn (2021), a geological model of the aquifer was derived and a steady state variable density groundwater flow model for the year 1968 was implemented into the groundwater modelling software GMS. In this study, the underlying groundwater flow model for constant density is extended to a transient model. Furthermore, additional adjustments are done to the underlying conceptual model to achieve a more accurate representation of the real system. Succeedingly, the model is calibrated for transient state in respect to a set of eleven model parameters. For this process however, the commonly used error measures *RMSE* and *MAE* are considered as theoretically unfit for assessment of time series. Therefore a set of three custom error measures is derived, which characterise the initial offset of simulated hydraulic heads, their long-term trends and the accuracy of the underlying assumptions in comparison to the observational data. With these measures, a sensitivity analysis and the subsequent calibration are executed. A final set of parameter values is obtained that fits the simulation values best to the observations. Finally, the custom error measures are compared to the *RMSE*. It is found that in this particular case both are equivalent. Finally it is concluded that even though no benefit on the result in the present application can be observed, the derived error measures however can improve calibrations in other cases when parameters show a higher level of interaction.

**Keywords** groundwater modelling · transient state · model calibration



# Résumé

Michael Weber

Étudiant à l'Université Leibniz de Hanovre  
weber@stud.uni-hannover.de

La plaine de Chtouka, dans le sud-ouest du Maroc, contribue de manière importante à la production agricole nationale. Comme elle est située dans une région au climat semi-aride, une irrigation extensive est nécessaire pour maintenir les cultures. En raison de l'absence de ressources en eau de surface suffisantes, la demande en eau est satisfaite par l'extraction des eaux souterraines de l'aquifère de Chtouka. Depuis le milieu du 20e siècle, la surexploitation des eaux souterraines a conduit localement à des baisses significatives de la nappe phréatique de 20 m et plus ces dernières années. Ce rabattement entraîne l'intrusion d'eau salée de l'océan Atlantique dans les zones côtières et un appauvrissement supplémentaires des ressources en eau douce disponibles. Au niveau administratif, un certain nombre de mesures ont été prises au cours des deux dernières décennies pour contrer cette évolution. Cependant, l'évaluation de ces mesures et les décisions de gestion futures dépendent fortement des informations sur l'état et la réponse de l'aquifère. Pour cela, les modèles d'écoulement d'eau souterraine se sont avérés être un instrument précieux pour prédire les impacts des mesures et des développements futurs.

Dans un travail précédent de Horn (2021), un modèle géologique de l'aquifère a été développé et un modèle d'écoulement des eaux souterraines à densité variable en régime permanent pour l'année 1968 a été implémenté dans le logiciel GMS (Groundwater Modeling Software). Dans cette étude, un modèle d'écoulement transitoire à densité constante pour 1968-2020 est développé sur la base du modèle de Horn (2021). En outre, des ajustements supplémentaires sont effectués sur le modèle conceptuel sous-jacent afin d'obtenir une représentation plus précise du système réel. Ensuite, le modèle est calibré en régime transitoire en ajustant onze paramètres. Cependant, les mesures d'erreur communément utilisées RMSE et MAE sont considérées comme théoriquement inadaptées à l'évaluation des séries temporelles. Par conséquent, un ensemble de trois mesures d'erreur spécifiques est dérivé, qui caractérise: le décalage initial des hauteurs hydrauliques simulées, leurs tendances à long terme et l'exactitude des hypothèses sous-jacentes par rapport aux données d'observation. Avec ces mesures, une analyse de sensibilité et la calibration en résultant sont effectuées. Un ensemble final de valeurs de paramètres est obtenu qui ajuste au mieux les valeurs de simulation aux observations. Enfin, les mesures d'erreur spécifiques sont comparées à la RMSE. Il s'avère que dans ce cas particulier, les deux sont équivalentes. Enfin, il est conclu que même si aucun avantage sur le résultat dans la présente application ne peut être observé, les mesures

d'erreur dérivées pourraient cependant améliorer les calibrations dans d'autres cas où les paramètres montrent un niveau d'interaction plus élevé.

**Mots clés** modélisation des eaux souterraines · régime transitoire · calibration de modèle

## **Declaration**

The present master thesis has been authored by Michael Weber.

It represents a student work, which has been developed under supervision of a scientific staff member at the “Federal Institute for Geosciences and Natural Resources (BGR)” in Hannover. Scientific findings presented in this study are student-based assessments and do not necessarily have to represent the appraisals of the Institute. This report is not a scientific publication and will not be permanently available as source of information.

I hereby declare that this master thesis „Numerical Investigation of Transient Water Flow in the Chtouka Aquifer, Morocco“ is the sole result of my independent research except where indicated by references to other sources and bibliography of other authors or by assistance of any kind. This study has not been presented to the Examination Authority or been published so far. I am aware that a false statement will have legal consequences.

Hannover, 06.10.2022

---



## Acknowledgements

I would like to thank my supervisor Dr. Nelly Montcoudiol, Federal Institute for Geosciences and Natural Resources (BGR), for the constant support and the valuable hints and advices throughout the work on this master thesis. I am grateful that you offered this many-sided topic and gave me the opportunity to gain interesting insights into a practical field. Furthermore I want to express my gratitude to Hendrik Schreiber, BGR, for openly asking critical questions during the technical meetings that made me reconsider ideas for the model and pointed me in the right directions.

I am glad that it was possible to write this thesis within this close cooperation between the BGR and the Institute of Fluid Mechanics and Environmental Physics in Civil Engineering (ISU). Many thanks are dedicated to the colleagues from the BGR, that welcomed me and helped me with my questions. I especially want to thank Dr. Ing. Sara Vassolo for the various help, not least in finding available workstations at the office and Dr. Georg Houben, who agreed on being my second examiner.

I want to thank apl.-Prof. Dr. Thomas Graf from the ISU for facilitating this external master thesis as first examiner and taking the time for the numerous regular meetings, which were invaluable for both the progress and the process, and once for again asking the right questions to keep me reconsidering.

Special thanks go to the colleagues from the Agence du Bassin Hydraulique du Souss Massa (ABHSM), Ms Fatima Abourrig, Mr Amine Touab and Mr Baba Sy from the OSS, who greatly worked on the project and enabled insightful meetings.

At last, I want to thank my family and friends, who always gave me support during my studies.



# Contents

<b>List of Figures</b>	<b>iii</b>
<b>List of Tables</b>	<b>vi</b>
<b>List of Abbreviations</b>	<b>viii</b>
<b>1 Introduction</b>	<b>1</b>
<b>2 Theoretical Background</b>	<b>3</b>
2.1 Fundamental Terms . . . . .	3
2.2 The Groundwater Flow Equation . . . . .	4
<b>3 Study Region: The Chtouka-Massa Plain</b>	<b>7</b>
3.1 Localisation . . . . .	7
3.2 Geology . . . . .	7
3.3 Climate . . . . .	9
3.4 Hydrology . . . . .	9
3.5 Economical Structure of the Region . . . . .	13
<b>4 Conceptual Model/Model Geometry</b>	<b>17</b>
4.1 Delineation of the Model . . . . .	17
4.1.1 Northern Boundary . . . . .	17
4.1.2 Eastern Boundary . . . . .	18
4.1.3 Southern Boundary . . . . .	20
4.1.4 Western Boundary . . . . .	22
4.2 Geological Model . . . . .	22
4.3 Recharge from Precipitation . . . . .	23
4.4 Groundwater Wells . . . . .	24
4.4.1 Drinking Wells . . . . .	25
4.4.2 Irrigation Wells . . . . .	25
4.5 Irrigation Returns . . . . .	26
4.6 Observations . . . . .	27
<b>5 Implementation of the Model</b>	<b>29</b>
5.1 Implementation of the Model . . . . .	29
5.1.1 Modelling Software: GMS . . . . .	29
5.1.2 Model Equations . . . . .	30

5.1.3	Implementation of the Conceptual Model in GMS . . . . .	30
5.1.4	Discretisation . . . . .	31
5.2	Methodology of Sensitivity Analysis and Calibration . . . . .	32
5.2.1	Examined Parameters . . . . .	34
5.2.2	Methodology of the Sensitivity Analysis . . . . .	36
5.2.3	Methodology of the Calibration . . . . .	37
5.2.4	Error Assessment . . . . .	38
<b>6</b>	<b>Results and Discussion</b>	<b>43</b>
6.1	Sensitivity Analysis . . . . .	43
6.2	Calibration . . . . .	50
6.3	Discussion of Error Measures . . . . .	50
6.4	Discussion Lumping of Irrigation Wells . . . . .	52
<b>7</b>	<b>Conclusion</b>	<b>53</b>
<b>Bibliography</b>		<b>55</b>
<b>A Task of the Master Thesis</b>		<b>59</b>

# List of Figures

4.6 Spatial distribution of the in this study considered 5498 irrigation wells (left) and 380 drinking wells (right). . . . .	26
5.1 Example of a two dimensional continuous parameter space $\Theta$ with elements $\boldsymbol{\theta} = (\theta_{1,i}, \theta_{2,j})$ . Each of these parameter sets corresponds to an absolute modelling error $\delta_{SM}$ marked by the colour scale. In this example, the parameter set $\boldsymbol{\theta}_{lo}$ corresponds to a local minimum of the modelling error $\delta_{SM}$ . The global optimum of $\delta_{SM}$ is obtained by the parameter set $\boldsymbol{\theta}_{go}$ . . . . .	34
5.2 (a): Time series of an observation and of three simulations with different parameter sets. In comparison with the observation all three simulations have an equal $RMSE$ . (b): Linear representation of the correlations between observed and simulated heads for the three simulations from (a). The respective data sets are each fitted with a linear (lin.) regression. The black dashed line marks identity between observed and simulated head. . . . .	39
6.1 Sensitivity of the model towards the parameter $K_h$ for all five materials $i$ , measured by the error $\Delta S_0$ . The corresponding parameter values $\theta_{i,j}$ are defined by Equation (5.25) and thus increase from left to right on a logarithmic scale. Each boxplot comprises the same set of piezometers. Whiskers and outliers are cut off for better perceptability. The black dotted lines mark the medians (+) and arithmetic means $\times$ of the reference parameter $\theta_{i,3}$ . . . . .	45
6.2 Sensitivity of the model towards the parameter $K_h$ for all five materials $i$ , measured by the error $p_1$ . The corresponding parameter values $\theta_{i,j}$ are defined by Equation (5.25) and thus increase from left to right on a logarithmic scale. Each boxplot comprises the same set of piezometers. Whiskers and outliers are cut off for better perceptability. The black dotted lines mark the medians (+) and arithmetic means $\times$ of the reference parameter $\theta_{i,3}$ . . . . .	45
6.3 Sensitivity of the model towards the parameter $K_h$ for all five materials $i$ , measured by the error $R^2$ . The corresponding parameter values $\theta_{i,j}$ are defined by Equation (5.25) and thus increase from left to right on a logarithmic scale. Each boxplot comprises the same set of piezometers. Whiskers and outliers are cut off for better perceptability. The black dotted lines mark the medians (+) and arithmetic means $\times$ of the reference parameter $\theta_{i,3}$ . . . . .	46

6.4 Sensitivity of the model towards the parameter $S_s$ for all five materials $i$ , measured by the error $\Delta S_0$ . The corresponding parameter values $\theta_{i,j}$ are defined by Equation (5.25) and thus increase from left to right on a logarithmic scale. Each boxplot comprises the same set of piezometers. Whiskers and outliers are cut off for better perceptability. The black dotted lines mark the medians (+) and arithmetic means $\times$ of the reference parameter $\theta_{i,3}$ . . . . .	46
6.5 Sensitivity of the model towards the parameter $S_s$ for all five materials $i$ , measured by the error $p_1$ . The corresponding parameter values $\theta_{i,j}$ are defined by Equation (5.25) and thus increase from left to right on a logarithmic scale. Each boxplot comprises the same set of piezometers. Whiskers and outliers are cut off for better perceptability. The black dotted lines mark the medians (+) and arithmetic means $\times$ of the reference parameter $\theta_{i,3}$ . . . . .	47
6.6 Sensitivity of the model towards the parameter $K_h$ for all five materials $i$ , measured by the error $R^2$ . The corresponding parameter values $\theta_{i,j}$ are defined by Equation (5.25) and thus increase from left to right on a logarithmic scale. Each boxplot comprises the same set of piezometers. Whiskers and outliers are cut off for better perceptability. The black dotted lines mark the medians (+) and arithmetic means $\times$ of the reference parameter $\theta_{i,3}$ . . . . .	47
6.7 Sensitivity of the model towards the parameter $\theta_{Q,irr}$ , measured by the error $\Delta S_0$ . The corresponding parameter values $\theta_{i,j}$ are defined by Equation (5.25) and thus increase from left to right on a logarithmic scale. Each boxplot comprises the same set of piezometers. Whiskers and outliers are cut off for better perceptability. The black dotted lines mark the medians (+) and arithmetic means $\times$ of the reference parameter $\theta_{i,3}$ . . . . .	48
6.8 Sensitivity of the model towards the parameter $\theta_{Q,irr}$ , measured by the error $p_1$ . The corresponding parameter values $\theta_{i,j}$ are defined by Equation (5.25) and thus increase from left to right on a logarithmic scale. Each boxplot comprises the same set of piezometers. Whiskers and outliers are cut off for better perceptability. The black dotted lines mark the medians (+) and arithmetic means $\times$ of the reference parameter $\theta_{i,3}$ . . . . .	48
6.9 Sensitivity of the model towards the parameter $\theta_{Q,irr}$ , measured by the error $R^2$ . The corresponding parameter values $\theta_{i,j}$ are defined by Equation (5.25) and thus increase from left to right on a logarithmic scale. Each boxplot comprises the same set of piezometers. Whiskers and outliers are cut off for better perceptability. The black dotted lines mark the medians (+) and arithmetic means $\times$ of the reference parameter $\theta_{i,3}$ . . . . .	49

- 6.10 The results of the calibration process for the error measures  $p_1$  and  $\Delta S_0$ . The *RMSE* is plotted for comparison. Along the  $x$ -axis advances the calibration process, starting on the left with the initial simulation results. All seven executed iterations are depicted. Of these, the first six are shown aggregated as final iteration result. For the last iteration, for each of the material parameters the best-fitting result is shown. The last four instances mark final variations of  $\theta_{Q,irr}$ .

# List of Tables

5.1	Overview of the in GMS implemented layers. Each layer is comprised of features of the specified object class and utilises the listed MODFLOW packages. (*): The time-dependent areas of the private perimeter are divided by corresponding periods into six layers (Section 5.1.1). . . . .	31
5.2	Overview of the value ranges of the parameters horizontal hydraulic conductivity $K_h$ and specific storage $S_s$ for all materials. Furthermore the value ranges of specific yield $S_y$ and material thickness $b$ are listed that were used to calculate the specific storages. . . . .	36
6.1	Summary of the sensitivities of the different error measures $p_1$ , $\Delta S_0$ and $R^2$ to the material-specific parameters $K_h$ and $S_s$ and the other parameter $\theta_{Q,irr}$ . Sensitivities are measured on the following ordinal scale: ++: highly sensitive, +: sensitive, o/+: sensitive in only single parameters, averages and medians not significantly affected, o: not significantly sensitive. . . . .	50
6.2	The values of final parameter set. . . . .	51



# List of Abbreviations

calc.	-	calcareous
GMS	-	Groundwater Modeling System
GPS	-	Global Positioning System
lin.	-	linear
m.a.s.l.	-	meter above sea level
MAE	-	mean average error
MODFLOW	-	modular finite-difference flow model
MT3DMS	-	Modular Transport, 3-Dimensional, Multi-Species model
PDAIRE	-	Plan directeur d'aménagement intégré des ressources en eau
PiT	-	point-in-time
RMSE	-	root mean squared error
TIN	-	triangulated irregular network
TS	-	time series
YBT	-	Youssef Ben Tachfine



# Chapter 1

## Introduction

In many, especially arid and semi-arid regions groundwater is a major source for drinking water, industrial use and agriculture. Due to intensification of agricultural activities and population growth, stresses on groundwater resources increased in recent decades (Choukr-Allah et al., 2017, El-Rawy et al., 2022). This has led to groundwater over-exploitation, inducing a decrease of groundwater tables with various consequences (Hsaisoune et al., 2017). One example is that former productive wells dried out, which raised the necessity of drilling new and deeper wells that are more costly (English, 1990).

Another effect can be saltwater intrusion in coastal aquifers (Fetter, 2001) - there, a natural balance exists between freshwater from inland and more dense saltwater from the ocean (Mays and Todd, 2005). If the groundwater table inland decreases due to groundwater overexploitation, this balance is disrupted (Fetter, 2001). In absence of counterpressure from the land side, saltwater pushes into the aquifer. Wells in proximity to the coast, that were previously pumping freshwater are contaminated, as they can succeedingly only provide saltwater (Fetter, 2001). This saltwater however is unfit for common agricultural use (Taiz et al., 2015) and other purposes.

Countermeasures to mitigate groundwater depletion can be the reduction of water usage. Therefore, modernisation of irrigation techniques to more water-efficient methods, implementation of deficit irrigation, reduction of tap water usage, increases of water cycle efficiencies in urban areas or the cultivation of different plant species with lower water demand are examples (English, 1990, Schütze et al., 2012). Second, the quantity of available freshwater resources can be increased, e.g. through operation of desalination plants in coastal areas or the import of water from other regions. Third, the microclimate conditions can be manipulated favourably through changes in land usage.

However, any of these countermeasures require detailed assessments of their particular plausibility and economical efficiency. Therefore, robust estimations of future water availability and the single measures', site-specific impact on water balances are required (El-Rawy et al., 2022). Therewith, possible scenarios can be developed. A valuable tool for precise estimations of impacts of possible measures are numerical models of the hydrological system (El-Rawy et al., 2022).

In this study, such a model is examined and further adjusted for the Chtouka aquifer. The Chtouka aquifer is located within the agriculturally important Souss-Massa River Basin in south-western Morocco. The Chtouka plain encompasses a major agricultural area. Freshwater is solely supplied by the Youssef Ben Tachfine (YBT) water reservoir and the Chtouka aquifer underlying the plain. In Chapter 3 this area is described in detail. In a previous study by Horn (2021), a steady state model was calibrated for the hydrological year 1968/69. It is implemented in the Groundwater Modelling System (GMS). In this study, it is expanded to a transient constant-density groundwater flow model. The conceptual model is presented and the adjustments made are described in Chapter 4. The implementation into GMS is then described in Chapter 5. For the sensitivity analysis and the calibration of the model, the common error measures root mean squared error ( $RMSE$ ) and mean absolute error ( $MAE$ ) are deemed to be inaccurate. Therefore, three custom error measures are identified and partially derived from considerations of the correlations between observations and simulation results (Chapter 5). These are coefficients describing the over- or underestimation of initial groundwater levels ( $\Delta S_0$ ), long-term trends ( $p_1$ ) and deviations from a linear correlation ( $R^2$ ). Finally, a sensitivity analysis of the implemented model is executed and the model is calibrated using the three error measures. The performance of the measures is then discussed and compared to the  $RMSE$ .

# Chapter 2

## Theoretical Background

### 2.1 Fundamental Terms

Rocks and soils constituting ground are commonly porous materials, consisting of a solid matrix and an interstitial pore space. Depending on the size of the pores, they can store and conduct groundwater. The ratio between the volume of the pore space  $V_p$  and the total volume  $V_{tot}$  of a soil probe is called the porosity  $\phi$  (Fetter, 2001),

$$\phi = \frac{V_p}{V_{tot}} \quad (2.1)$$

The accessibility of the pore space to water and to a water flow is limited by the pores of smallest diameter, thus possibly creating non-water filled pores and dead ends. Therefore, only a smaller portion of the pore space is effectively available for groundwater flow. This portion of the pore space is called the effective porosity  $\Phi_{eff}$  (Fetter, 2001). It is defined as the ratio of the water-available volume  $V_w$  to the total volume of a soil probe,

$$\Phi_{eff} = \frac{V_w}{V_{tot}} \quad (2.2)$$

On mechanical level, the water contained in a soil interacts with the solid matrix amongst others through molecular and surface tension forces. In case of gravitational drainage of an initially saturated soil, gravitation exerts a stress on the water film enclosing the matrix elements. As the stored water volume decreases, surface tension increases until a balance of the two opposing stresses reaches an equilibrium (Fetter, 2001). The water volume drained through gravitation is called the gravity groundwater, with the corresponding volume being denoted by  $V_{w,g}$  (Johnson, 1967). The ratio between  $V_{w,g}$  and the total volume  $V_{tot}$  is called the specific yield  $S_y$ ,

$$S_y = \frac{V_{w,g}}{V_{tot}} \quad (2.3)$$

Another stress on a water-filled soil stems from the pressure exerted by the water column, which is measured as hydraulic head. Due to the elasticity of both the solid matrix and the water in the voids this leads to a variability of the amount of stored water (Fetter, 2001). For one, an increasing pressure induces a contraction of the solid matrix and thus increases the effective porosity. Additionally the water itself is compressed in this case, thereby allowing for more water to be stored. The specific storage  $S_s$  (m) accounts for this effect. It is defined by

$$\frac{\partial \rho \phi}{\partial t} = \rho g (\beta_p + \phi \beta_w) \quad (2.4)$$

with the density  $\rho$  ( $\text{kg m}^{-3}$ ) of water, the standard gravity  $g$  ( $\text{m s}^{-2}$ ), the compressibility of the bulk aquifer material  $\beta_p$  ( $\text{m}^2 \text{N}^{-1}$ ) and the compressibility of water  $\beta_w$  ( $\text{m}^2 \text{N}^{-1}$ ). Specific yield and specific storage represent two different material properties of an aquifer. They are summarised by the dimensionless storativity  $S$  (Fetter, 2001),

$$S = S_y + b S_s \quad (2.5)$$

where  $b$  denotes the water-filled thickness of the aquifer. Graphically, the storativity is the volume of water  $V_w$  absorbed or expelled from storage of a permeable unit per unit surface area  $A$  and unit change in head  $h$  (Fetter, 2001),

$$S = \frac{1}{A} \frac{\partial V_w}{\partial h} \quad (2.6)$$

For unconfined aquifers the contribution from the specific yield is much larger than the contribution from the specific storage to the storativity (Todd and Mays, 2005). For draining confined aquifers however, the specific yield equals zero as long as they remain water saturated (Fetter, 2001). Thus, the specific storage of a confined aquifer can be approximated by

$$S_s = \frac{S}{b} \quad (2.7)$$

## 2.2 The Groundwater Flow Equation

For water flowing in an aquifer conservation of mass can be assumed (Mays and Todd, 2005). Furthermore, the aquifer can be divided into a number of small control volumes  $dV = dx dy dz$  with side lengths  $dx$   $dy$  and  $dz$  in  $x$ -,  $y$ - and  $z$ -direction, respectively (Fetter, 2001). On each of these control volumes a mass balance can be written, where the change in stored mass  $dM/dt$  in the volume over time equals the difference in rates

of inflowing water mass  $\dot{M}_{in}$ , outflowing water mass  $\dot{M}_{out}$  and water mass added or withdrawn by sources or sinks  $\dot{M}_{ss}$ ,

$$\frac{dM}{dt} = \dot{M}_{in} - \dot{M}_{out} + \dot{M}_{ss} \quad (2.8)$$

The mass flow rates can also be written in terms of water density  $\rho(\mathbf{x}, t)$  and fluxes  $\mathbf{q} = (q_x, q_y, q_z)$  through the surfaces  $(dx dy)$ ,  $(dx dz)$  and  $(dy dz)$  of the control volume (Mays and Todd, 2005). Assuming a constant density  $\rho(\mathbf{x}, t) = \rho$  and letting the side lengths tend towards zero gives

$$\frac{dM}{dt} = \rho dx dy dz \left( \frac{\partial q_x}{\partial x} + \frac{\partial q_y}{\partial y} + \frac{\partial q_z}{\partial z} \right) \quad (2.9)$$

With Darcy's law the fluxes  $q_i$  can be estimated through the changes  $\partial h / \partial x_i$  in hydraulic head  $h$ ,

$$q_i = \sum_{j=x,y,z} \left( K_{ij} \frac{\partial h}{\partial x_j} \right) \quad (2.10)$$

where  $K_{ij}$  denote the respective hydraulic conductivities (Mays and Todd, 2005). Without loss of generality the coordinate axes of the control volume can be chosen parallel to the major directions of the porous medium, so that the non-diagonal terms of the hydraulic conductivity tensor equal zero,  $K_{ij} = 0 \forall i \neq j$ . Therewith Equation (2.9) becomes

$$\frac{dM}{dt} = \rho dx dy dz \left( \frac{\partial}{\partial x} \left( K_{xx} \frac{\partial h}{\partial x} \right) + \frac{\partial}{\partial y} \left( K_{yy} \frac{\partial h}{\partial y} \right) + \frac{\partial}{\partial z} \left( K_{zz} \frac{\partial h}{\partial z} \right) \right) \quad (2.11)$$

The stored water mass  $M$  on the left hand side is generally given by the density of water  $\rho(\mathbf{x}, t)$  and the water volume inside the control volume. This volume is given according to Equation (2.2) by the effective porosity  $\phi_{eff}$  and the total volume of the control volume  $dV = dx dy dz$ ,

$$M = \rho(\mathbf{x}, t) \phi_{eff} dV \quad (2.12)$$

Here  $dV$  is by definition constant over time. However both water density and effective porosity depend on the stresses exerted on the control volume and are therewith functions of space and time. Thus follows

$$\frac{dM}{dt} = dV \frac{\partial(\rho(\mathbf{x}, t) \phi_{eff})}{\partial t} \quad (2.13)$$

Through application of the chain rule the right side can be expressed through the specific storage  $S_s$  and the change in hydraulic conductivity (Mays and Todd, 2005). As for Equation (2.9) constant density  $\rho$  is assumed. This ultimately leads to the groundwater flow equation (Mays and Todd, 2005):

$$S_s \frac{\partial h}{\partial t} = \frac{\partial}{\partial x} \left( K_{xx} \frac{\partial h}{\partial x} \right) + \frac{\partial}{\partial y} \left( K_{yy} \frac{\partial h}{\partial y} \right) + \frac{\partial}{\partial z} \left( K_{zz} \frac{\partial h}{\partial z} \right) + \dot{M}_{ss} \quad (2.14)$$

# **Chapter 3**

## **Study Region: The Chtouka-Massa Plain**

### **3.1 Localisation**

The study area is located bordering the Atlantic Ocean and is part of the over 27 000 km<sup>2</sup> extending Souss-Massa Basin in south-western Morocco (Figure 3.1). The Souss-Massa Basin comprises the watersheds of the rivers Souss in the north and north-east and Massa in the south. The former originates in the mountains of the High Atlas to the north, the Siroua Massif to the east and the Anti Atlas to the south-east, and the latter in the Anti Atlas to the east and south-east. These mountains and their foothills constitute the boundaries of the basin to the north, east and south-east, while the Atlantic Ocean forms its boundary to the west. Below 700 m.a.s.l. and down to 0 m.a.s.l. the triangular-shaped, extensively agriculturally developed Souss plain lies embedded between the mountains and has an area of 5 700 km<sup>2</sup> (Choukr-Allah et al., 2017).

In this study, a model for the Chtouka aquifer is examined. The Chtouka aquifer underlies the agriculturally important Chtouka plain. It is localised within the Souss-Massa plain near the western coast, and has an area of 1 300 km<sup>2</sup> (Figure 3.1). The Chtouka plain ranges approximately from 0 m.a.s.l. on the western Atlantic coast up to 348 m.a.s.l. in the south-eastern mountainous area. Sloping from east to west, 80 % of its surface is between 50 and 175 m.a.s.l..

### **3.2 Geology**

The Souss-Massa plain has been formed by the homonymous rivers and their tributaries and is covered by their alluvial deposits (Hssaisoune et al., 2017). These alluvial deposits are porous and constitute an aquifer. The Chtouka aquifer can be characterised by four different major Plio-Quaternary geological formations according to Malki et al. (2017):

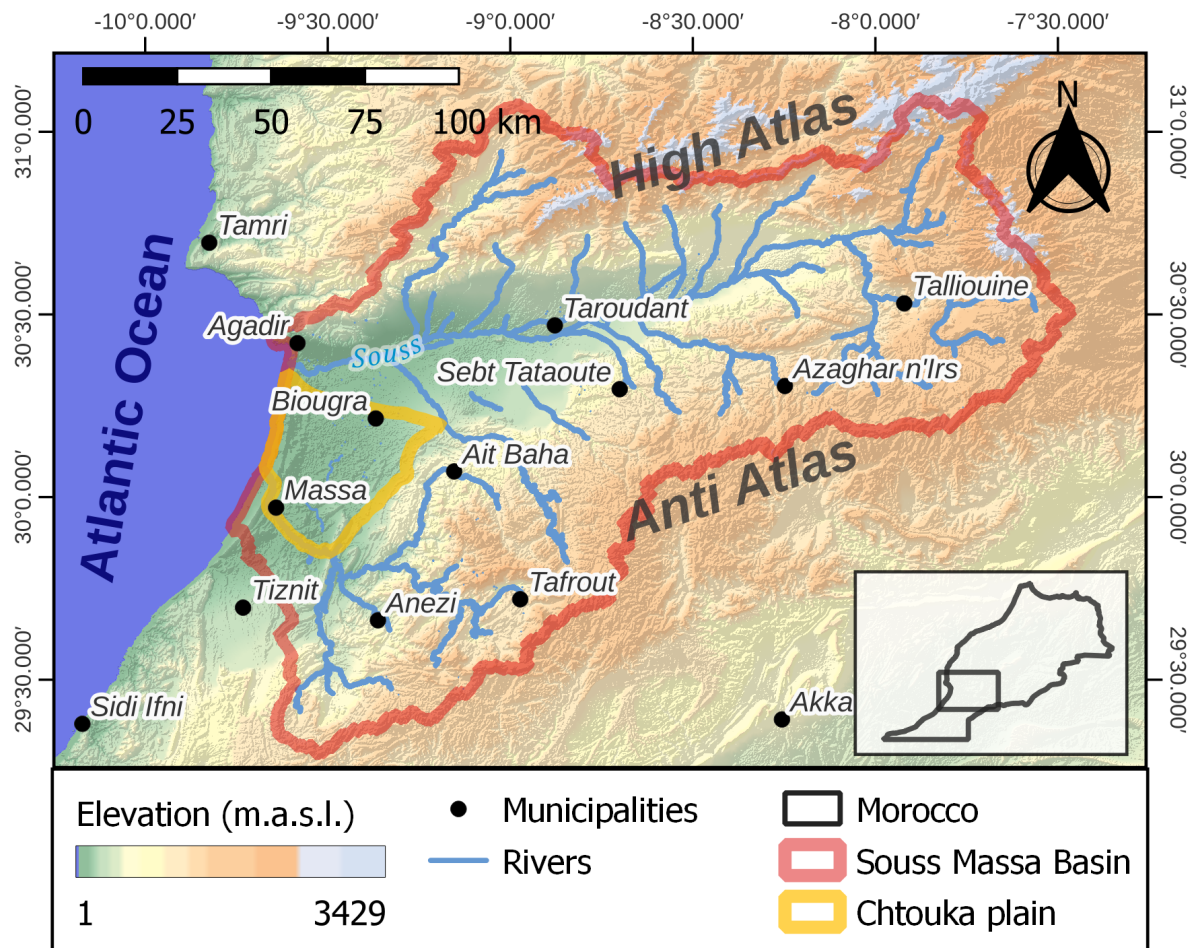


Figure 3.1: Map of the Souss-Massa Basin, showing the location the Chtouka plain. This representation is derived from digital elevation model data of NASA JPL (2013) and follows in topographical colouring Hssaisoune et al. (2017).

- (i) in the southern and eastern parts of the plain marls and limestones basing directly on Acadian age schist,
- (ii) conglomeratic deposits in the beds of the Massa,
- (iii) sands and silts as alluvial deposits from the recent Quaternary and
- (iv) lacustrine limestones with large spatial extension.

For further information, see Choubert, 1964, Hssaisoune et al., 2017, Horn, 2021 and Krimissa et al., 2004.

### **3.3 Climate**

Generally, climatic conditions in the Souss-Massa Basin are semi-arid (Choukr-Allah et al., 2017). However, some spatial variability can be observed. In the Souss-Massa plain annual rainfall averages at around  $250 \text{ mm a}^{-1}$ , while in the mountains average annual rainfalls are at around  $600 \text{ mm a}^{-1}$ . This leads to the surface water supply in the plain being higher than its local climate may suggest (Hssaisoune et al., 2017). Annual rainfalls over the last decades in Biougra, in the Chtouka plain (Figure 3.2) and a climate chart for the region are shown in Figure 3.3. According to this chart and following the modified Köppen system as described in Critchfield (1983), the Chtouka area has a semi-arid climate (Choukr-Allah et al., 2017). In the Chtouka area, the long-term average precipitation is about  $187 \text{ mm a}^{-1}$  (Figure 3.3(b)).

Over the years, precipitation show a high variability between years with over  $600 \text{ mm a}^{-1}$  (three times the long-term average) in humid years and less than  $50 \text{ mm a}^{-1}$  (a quarter of the long-term average) in dry years. Potential evapotranspiration on the other hand lies at approximately  $2000 \text{ mm a}^{-1}$  in the Souss Massa Basin (Choukr-Allah et al., 2017) and therewith significantly exceeding water supplies through rainfall, as typical for arid and semi-arid climates. It may be noted that as basis for yearly measurements the local hydrological year is from 1st of September to 31st of August of the following year. Following this convention, in this work this specific hydrological year is always implied, whenever a "year" is referenced. For ease of reading however, instead of the full label (e.g. "2021-22") only the first calendar year will be shown in labels ("2021").

### **3.4 Hydrology**

In the Souss-Massa Basin, in average  $1093 \text{ Mm}^3$  of water are available according to ABHMSM (as cited by Choukr-Allah et al. (2017)), consisting of 36 % surface water and 64 % groundwater (Choukr-Allah et al., 2017). Surface water is mainly provided by the two homonymous rivers. Depending on the yearly rainfall, surface water potential shows a large variability from year to year (Choukr-Allah et al., 2017, ABHSM, 2022c).

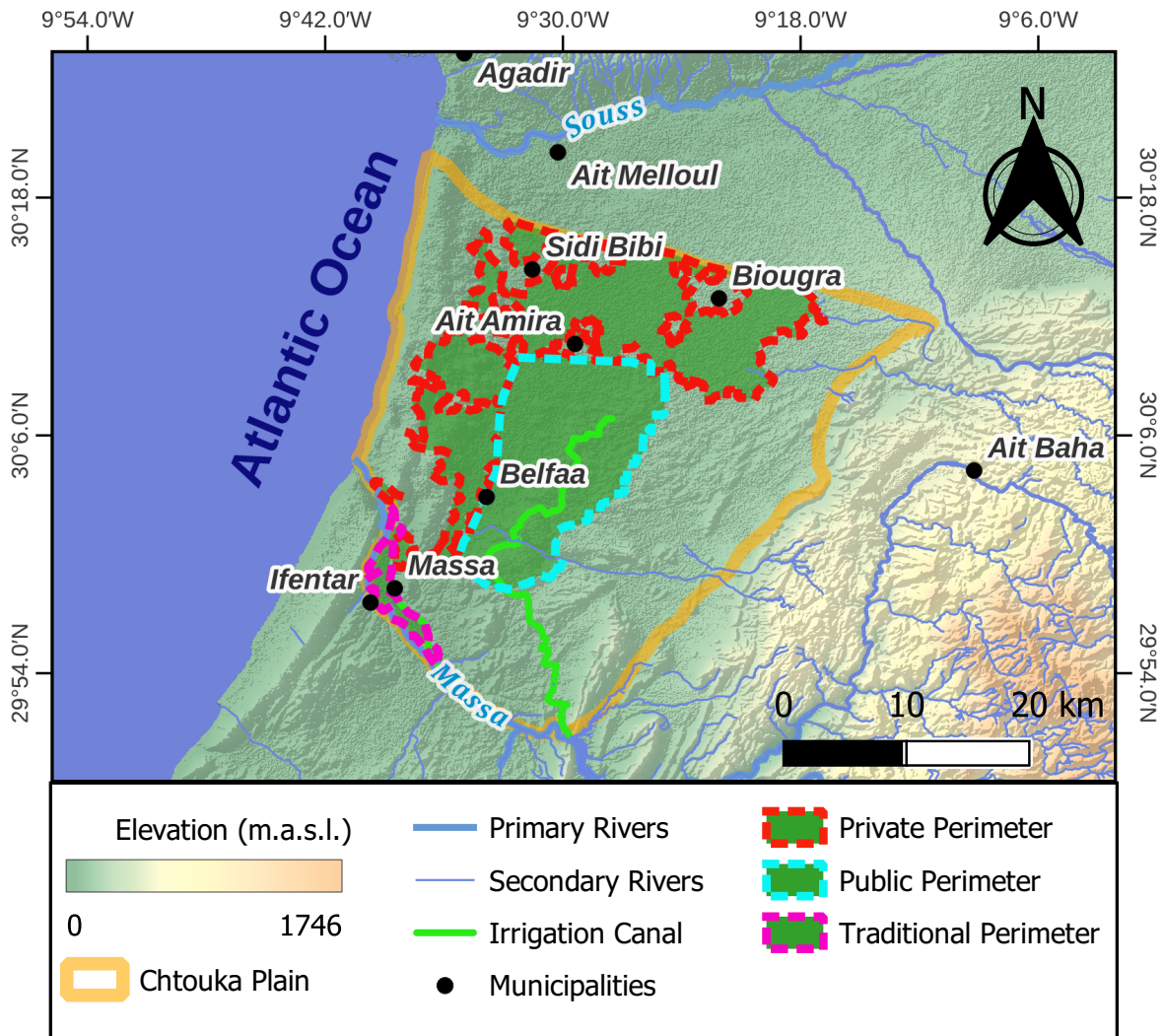


Figure 3.2: Map showing the Chtouka plain and its irrigation perimeters. The map is derived from the digital elevation model data of NASA JPL, 2013.

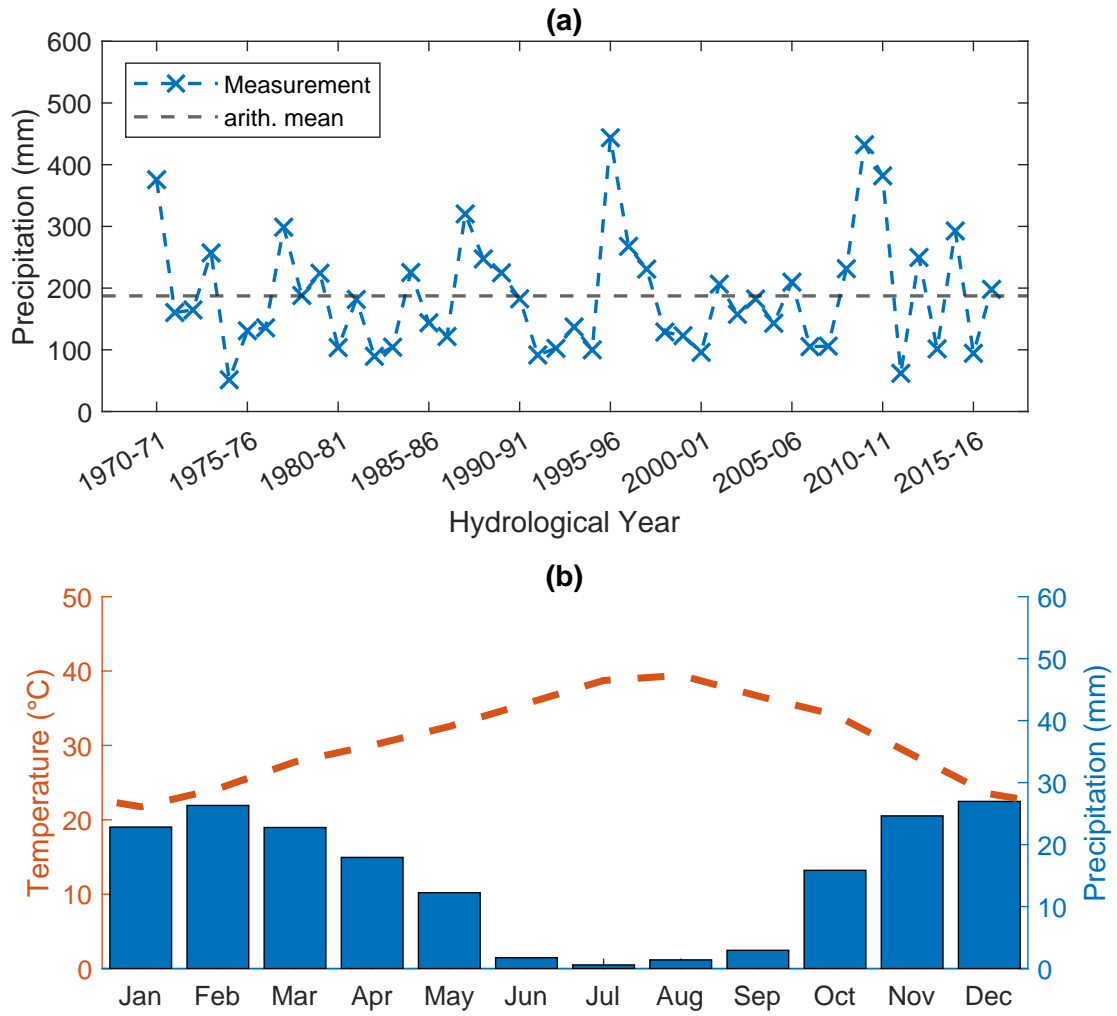


Figure 3.3: Climatic conditions in the Chtouka-Massa plain. (a): Annual precipitations at the city of Biougra for the period 1970 to 2016. Measurement periods are the respective hydrological years, which range from 1st of September of the denoted year to 31st of August of the following year. The underlying dataset was provided by the ABHSM. (b): Long-term average temperatures and precipitation during a year. The climate chart bases on data for the years 1950-2017 and is derived from the globally gridded monthly time series datasets by Matsuura and Willmott (2018a) and Matsuura and Willmott (2018b).

To regulate the flows of both rivers and ensure a regular supply of water in the Souss-Massa Basin, a total of eight dams have been built in the period from 1972 to 2004 (Choukr-Allah et al., 2017). These dams have a total potential capacity of 730 404 Mm<sup>3</sup>. Of these, the Youssef Ben Tachfine (YBT) dam which was put into service in 1972 and is functioning since 1974, is the largest with a potential capacity of approximately 300 000 Mm<sup>3</sup> (ABHSM, 2022b). It is located in the south-east of the Chtouka plain (Figure 3.2).

The Souss River originates to the north in the High Atlas mountains where its tributaries form a dense drainage network and to the south in the Anti Atlas where the tributary network is lighter (Hssaisoune et al., 2017). After confluencing from its different tributaries, the river flows from east to west over 182 km through the Souss plain, from which it ultimately discharges to the west into the Atlantic Ocean near Agadir (Figure 3.1). Its flow is strongly seasonal, and during rainy years high floods can occur between October and February (Hssaisoune et al., 2017).

The Massa River, which forms the southern boundary of the Chtouka plain, originates in the Anti Atlas mountains, from where it flows in western to north-western direction towards the Atlantic Ocean. At the southern-most corner of the aquifer it supplies the biggest reservoir of the Souss Massa Basin, the Youssef Ben Tachfine (YBT) dam, which regulates the Massa River on the 36 km of its course to the Atlantic Ocean. Downstream of the dam, the river first flows in a small, steep-sided channel of 5 to 10 m width with a rather steep topographic gradient. Subsequently when reaching the Massa plain near Ifentar it flows in a wider, meandering channel (Horn, 2021). The Massa River exhibits a high variability following annual and interannual climatic irregularities characterised by brief floodings interrupted by long periods of dryness (Hssaisoune et al., 2017).

An irrigation canal originating from the YBT dam supplies water to an agricultural area in the centre of the Chtouka plain (Figure 3.2), which is called the public irrigation perimeter. This area is surrounded to the north and west by the private irrigation perimeter. Another channel, originating downstream of the YBT dam supplies the Tassila agricultural area near Massa municipality. Furthermore, water from the reservoir is used for drinking water supplies of Tiznit and Ifni.

Overall, the principal water resources of the Souss-Massa Basin are the groundwater and the eight dams (Hssaisoune et al., 2017). The groundwater reservoir is situated solely below the Souss-Massa plain and therewith only up to 700 m.a.s.l., as the higher parts are mountainous. These mountainous areas form major recharge areas of the aquifer.

Although water supply in the Souss Massa Basin consist of both surface water in the homonymous two rivers and their tributaries as well as groundwater from the aquifer, in the Chtouka area groundwater constitutes the major water source. Surface water mostly consists of the Massa River along its southern boundary and the irrigation canal supplied by the YBT dam. Following very intense precipitation events, some intermittent wadis flow from the Anti Atlas mountains into the Chtouka plain.

In the Souss Massa Basin, water demand is composed of 12.5 % drinking water and water for industrial use, and 86 % for agricultural purposes (Choukr-Allah et al., 2017). The water demand is seasonal, as irrigation and tourism are in summer more extensive, while at the same time natural water supply is minimal (Choukr-Allah et al., 2017). In the hydrological year 2018 the YBT dam supplied 51 018 Mm<sup>3</sup> for irrigation and 8 208 Mm<sup>3</sup> for drinking purposes (ABHSM, 2022c).

In the Souss Massa Basin water exploitation increased significantly in the last decades due to increased irrigated agriculture, tourism and industrial development (Choukr-Allah et al., 2017, Hssaisoune et al., 2017). Therefore groundwater levels decreased over the past four decades within a range of 0.5 – 2.5 m a<sup>-1</sup> due to overpumping (Choukr-Allah et al., 2017) (Hssaisoune et al., 2017). This led to deterioration of groundwater due to saltwater intrusion in coastal areas and deep well drilling over the past decade (Choukr-Allah et al., 2017).

For the Chtouka aquifer, the water imbalance between recharge and withdrawal of groundwater evaluated to be 58 Mm<sup>3</sup> a<sup>-1</sup> in 2007 (ABHSM, 2022a). Furthermore the quality of the water resources degraded in the course of the last decades due to pollution mainly stemming from domestic, industrial and agricultural wastewaters and fertilisers. For example, nitrate concentrations exceed the regulatory threshold value of 50 mg l<sup>-1</sup> for drinking water in 36 % of the wells in the Chtouka plain (Choukr-Allah et al., 2017). In the next decades water demand is expected to further increase in the whole region due to population growth, increase in per capita consumption and extension of irrigated agriculture (Choukr-Allah et al., 2017). Simultaneously a decline in water availability is expected due to overpumping of groundwater and lower recharge through rainfalls, which in turn is caused by developing urbanisation and climate change (Choukr-Allah et al., 2017 Hssaisoune et al., 2017). To tackle these issues, in 2008 the "Plan directeur d'aménagement intégré des ressources en eau (PDAIRE)" was published. Besides a revised and intensified management of available water resources and the efficiency enhancement of water consumption, it aims at the exploitation of unconventional water resources such as wastewater reuse and the desalination of seawater (Choukr-Allah et al., 2017).

### 3.5 Economical Structure of the Region

Climate conditions in the Souss-Massa Basin provide conditions for a characteristic all-year round growing season (Hssaisoune et al., 2017). Therefore, the area is extensively used for agricultural production. On national level, agriculture has a growing contribution to the Moroccan gross domestic product (GDP), from 7 % in 1998-2008 to 17 % in 2008-2018 and thus plays a key role in Morocco's economical development (MAP-MDREF, 2021). In this sector the Souss-Massa plain is economically the second most important region in Morocco (Choukr-Allah et al., 2017). The economy of the region is

primarily founded on the high-value agricultural production, tourism and fishery. Covering more than one fifth of this area the Chtouka plain accounts for a significant portion of the agricultural production of the region (Choukr-Allah et al., 2017).

On administrative level, the Chtouka plain is part of the Chtouka-Ait Baha province, which reaches to the east past the plain and further into the Anti Atlas mountains. In this province a total population of 371 102 people was counted in 2014, of which 113 531 people lived in one of the four urban centres (Ait Baha, Biougra, Belfaa, Massa) and the rest in the 18 rural communes (DRSM, 2020). In the period between 2004 and 2014 the population of the province had an average annual growth rate of 2.24 % (DRSM, 2020). As shown by these numbers, the Chtouka plain is primarily a rural region.

With a year-round growing season, the Souss Massa Basin accounts besides other products for more than half the production of Moroccan citrus and vegetables (Hssaisoune et al., 2017). In the Chtouka plain, tomatoes and peppers are cultivated in greenhouses (DRSM, 2020) and furthermore other vegetables and fruits, cereals, fodders, ornamental crops and deciduous trees (Office Regional de Mise en Valeur Agricole de Souss-Massa, as cited by Malki et al., 2017). Surveys from 2015 identified a total number of 2724 farms covering an area of approximately 24 800 ha and which employ more than 40 000 people (ABHSMD, 2015, as cited by Choukr-Allah et al., 2017). The majority of these farms are located around Ait Amira, Belfaa, Biougra, Sidi Bibi and Massa (Figure 3.2). Like the whole region of the Souss Massa Basin (Choukr-Allah et al., 2017), irrigated areas in the Chtouka-Massa plain show an continuous expansion in the past decades.

In the area, three different irrigation practices are being used: flooding, sprinkler and drip irrigation. These different irrigation techniques exhibit different water usage efficiencies, with flooding being the least and drip irrigation being the most efficient. Simultaneously, these methods require a different technological development and therewith investment of farms, which is why their application highly depends on the economical organisation and situation of the farms (Choukr-Allah et al., 2017). Thus, the implementation of the different techniques varies both spatially and temporally over the agricultural area. Due to the problem of overexploitation of water resources (see Section 3.4), and following the agricultural strategy plan "Plan Maroc Vert" which was adopted in 2008 and its National Irrigation Water Saving Program, efforts have been made to significantly increase the portion of water efficient drip irrigation in the past 15 years (MAPMDREF, 2021). For instance, in the northern and north-western private perimeter where structured agri-business farms predominate, an extensive conversion to drip irrigation took place in recent years (ABHSMD, 2015, as cited by Choukr-Allah et al., 2017). At the same time, in the centrally located public perimeter sprinkler irrigation is still the predominant method. Furthermore, in these two perimeters cultivation widely takes place in greenhouses. At the traditionally farmed Tassila perimeter in the south, along the Massa River, water-intensive flooding is still the major technique. The extents of the private perimeter varied over the decades, whereas the public and traditional perimeter remained in constant extents. Their respective estimated boundaries

for the period 2010-2019 are shown in Figure 3.2.



# Chapter 4

## Conceptual Model/Model Geometry

Based on the descriptions of the preceding Chapter 3, the conceptual model of the Chtouka aquifer can be regarded as shown in Figure 4.1: First, groundwater directly enters and leaves the volume of the aquifer at its boundaries. Additional recharge is naturally provided by local rainfalls and infiltration from the Massa River, as well as from the YBT reservoir. At the same time, the Massa River can act as a drain of the aquifer, depending on its water level. Artificially, water is withdrawn for drinking and irrigation. As the irrigation water is applied to the irrigation perimeters at the surface of the aquifer, a fraction of the irrigation water reinfiltates into the aquifer. The other part is lost due to evapotranspiration.

In this chapter the conceptual model in Figure 4.1 is described. Therefore, the aquifer is first delineated and its boundaries are characterised (Section 4.1). Then the geological model of the aquifer volume is described, as it was derived by Horn (2021) (Section 4.2). In the subsequent Sections 4.3-4.5 the other sources and sinks of the water balance are specified. At last, in Section 4.6 the piezometers, which represent the observation points of the model are described.

### 4.1 Delineation of the Model

For delineation in the  $xy$ -plane, a set of four boundaries, each characterised by a particular type of boundary condition were defined (ANZAR CONSEIL, 2016). These different boundaries approximately follow the cardinal directions and are therefore named as *northern*, *eastern*, *southern* and *western boundary*. The four boundaries are shown in Figure 4.2. Their exact course is defined by ANZAR CONSEIL (2016).

#### 4.1.1 Northern Boundary

The northern boundary is defined as a Neumann no-flow boundary (Figure 4.2). It follows an estimated streamline derived from a contour map of the groundwater table in 1968 by Bernet (1968) (reproduced in Bernet and El Hebil, 1977) which represents

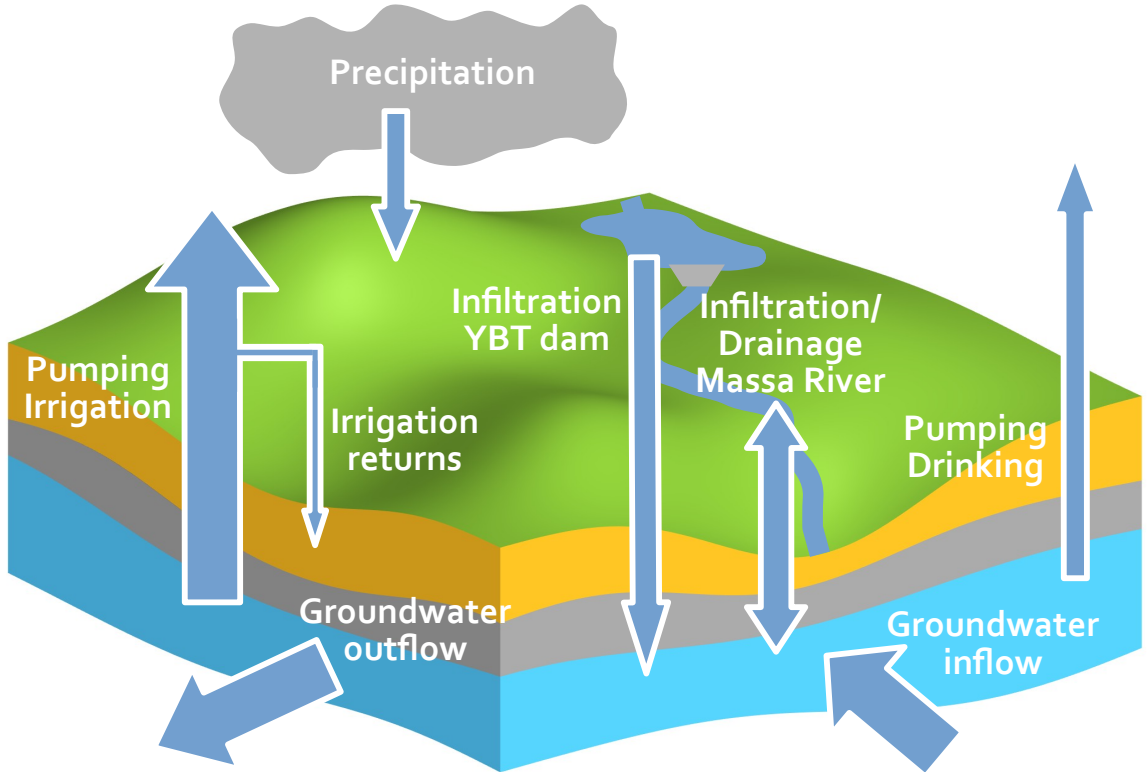


Figure 4.1: The conceptual water balance of the system.

a groundwater divide. The boundary runs from the north-eastern corner of the model over 45.3 km in north-western direction to the coast of the Atlantic Ocean. Even though streamlines change depending on groundwater levels and their spatial and temporal variation, due to lack of data this boundary is assumed to be constant over the modelling period.

### 4.1.2 Eastern Boundary

For this study, at the eastern boundary an adjusted version of the specified head boundary (Dirichlet) by Horn (2021) is used with estimated transient heads. This boundary marks the transition between the Chtouka plain and the foothills of the Anti Atlas (Figure 4.2). The head stages along the boundary vary in both space and time. They are estimated from surface elevation data of a digital elevation model (DEM) (NASA JPL, 2013) and piezometric measurements of the depth to the water table. These latter piezometric measurements were taken at different times and are within a 1.5 km wide buffer zone along the boundary. Most of the observations stem from initial measurements done when bringing new groundwater wells into service, and are single point-in-time measurements. This data encompasses two measurements from 1967 and therewith from

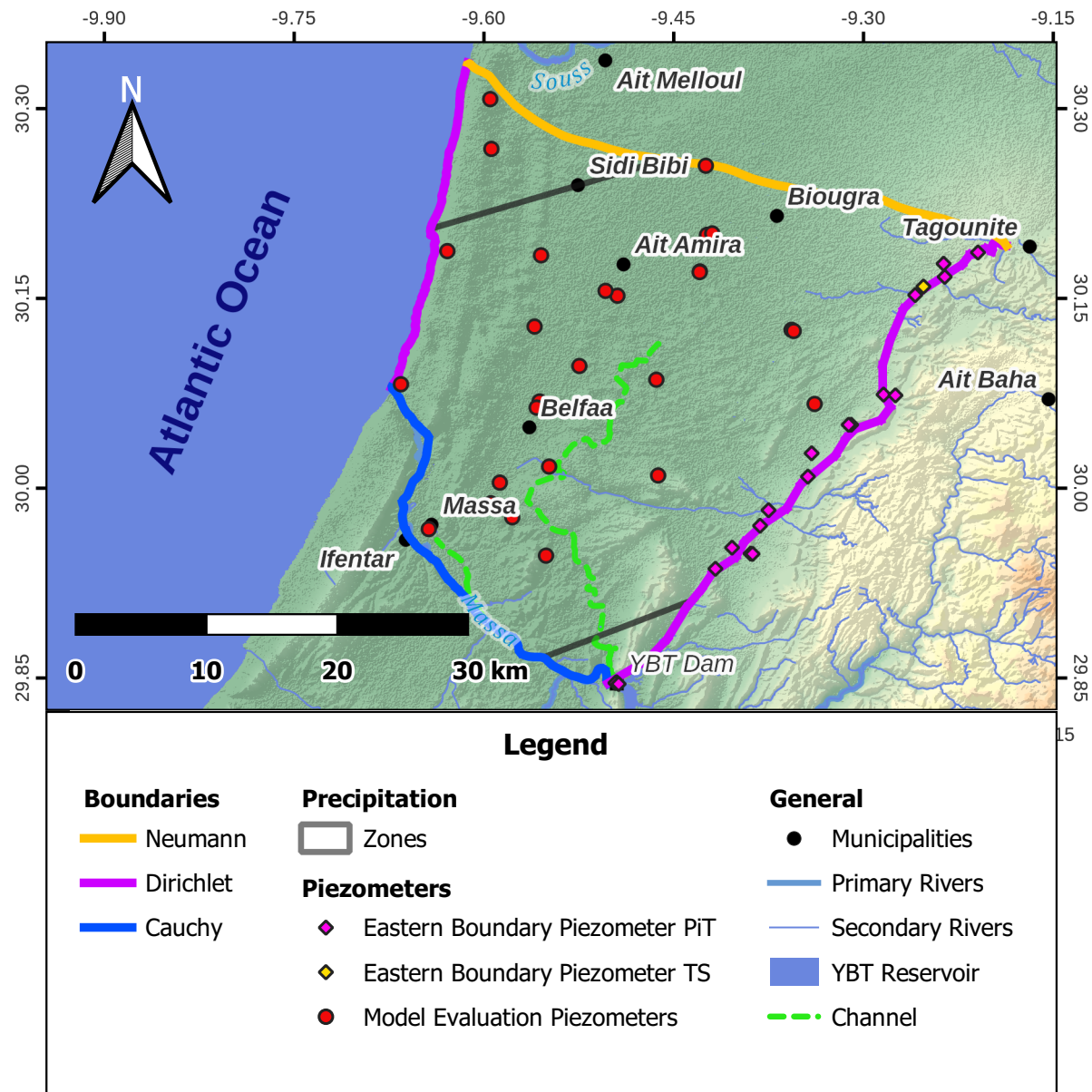


Figure 4.2: Main components of the Chtouka aquifer conceptual model. For clarity, only the boundaries separating the three precipitation areas are depicted. For the piezometers used to define the eastern boundary condition, PiT means point-in-time measurements and TS time series.

one year before the start of the modelling period. For the period from 1968 to 2003 a total of 14 more such measurements at different locations are available. Furthermore, at one location 8 km from the north-eastern corner of the model area a time series exists, covering the hydrological years 1968 to 1995 with a temporal resolution ranging from monthly to once every two years. Another much shorter time series, with a coverage of 10 measurements over 1.5 years, is considered as single point-in-time measure due to its only little variation of less than 1 m.

With these data the initial head in 1968 is estimated at 29 locations along the boundary based on three characteristics:

- (i) measurements from 1968,
- (ii) extrapolated measurements from earlier and later hydrological years, such that the amplitude of head variations over the years is of the same order as the one observed in the time series, and
- (iii) following the natural topography.

In between these 29 locations, heads are linearly interpolated along the boundary. The result is shown in Figure 4.3. From this initial boundary condition, using the available observations the temporal evolution of heads at the boundary is estimated for the hydrological years 1985, 1995 and 2005. In between these years, a linear evolution of the heads is considered. For the period after 2005 no further information is available and thus the heads are then assumed as constant.

### 4.1.3 Southern Boundary

The southern boundary is defined by the Massa River (Figure 4.2). Due to both the temporal and spatial variability of the flow regimes along the river, changing influent and effluent conditions of the aquifer occur along this boundary. To account for this, Horn, 2021 implemented this boundary as Cauchy boundary condition into GMS. Hence it is characterised through three parameters: the bottom elevation of the river channel, the head stage and the riverbed conductance. The bottom elevation is approximated using the DEM.

The head stages are estimated by an assumed linear relation between the discharge rate measured at the YBT dam and the assumed average water level in the river. These discharge rates are extracted from data of daily water balances in the YBT reservoir aggregated to yearly data. As these measurements were taken only from 1974 onwards, once the dam became fully operational, two different time periods need to be distinguished: before and after 1974. From 1968 to 1974 head stages are estimated from annual rainfalls.

The conductance  $C$  ( $\text{m s}^{-1}$ ) is estimated as conductance per unit length by

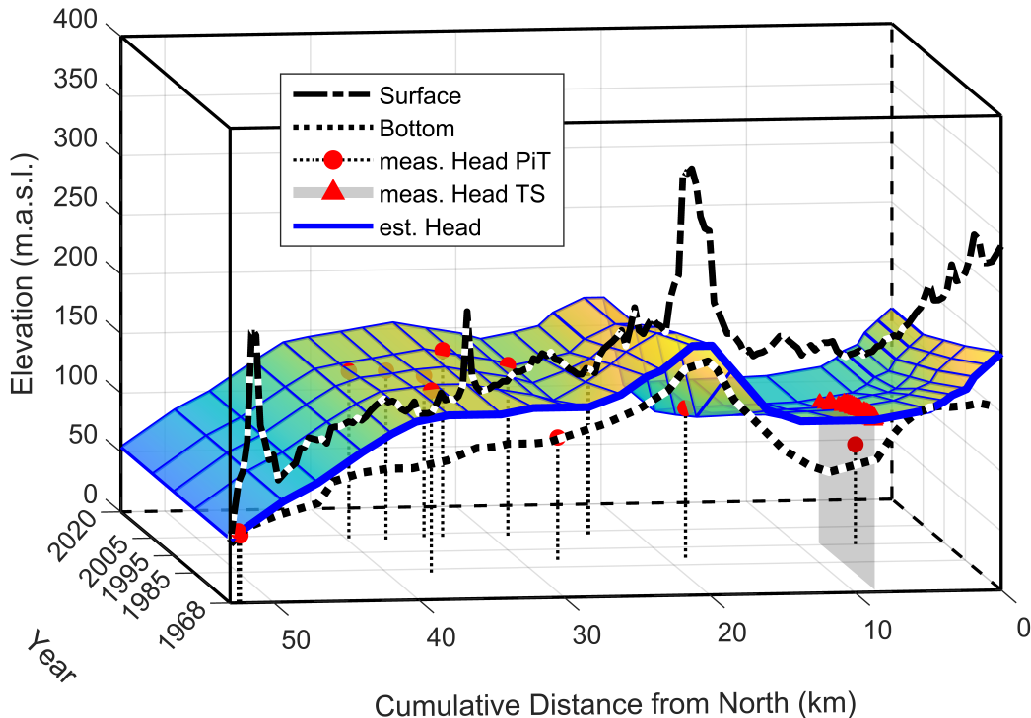


Figure 4.3: The adjusted Dirichlet boundary condition for the eastern boundary. The for 1968 estimated initial head (thick blue line) along with the bottom- (thick black dotted) and surface- (thick black dashed) elevations are shown at the starting year 1968. Measured heads are shown in red as circles for single point-in-time (PiT) measurements and as triangles for time series (TS) measurements. The grid (blue) spanning the temporal evolution of heads shows the linear interpolation in between the 29 locations and the five specified years. For better perceptability the surface marking the head stages in between these points is coloured according to head values.

$$C = \frac{k}{t}w \quad (4.15)$$

where  $k$  ( $\text{m s}^{-1}$ ) is the hydraulic conductivity of the riverbed,  $t$  (m) the riverbed thickness and  $w$  (m) the width of the river (Aquaveo, 2019). For the hydraulic conductivity values lower than those of the underlying lithological unit are assumed, as sedimentation may lead to clogging processes.

As described in Section 3.4, the Massa River can be divided into two different parts (Horn, 2021): an upstream part ranging from the YBT dam to the village of Ifentar, and a downstream part from Ifentar to the Atlantic Ocean. Therefore, on these two sections different assumptions define the applied parameters of river width and riverbed thickness. Higher flow velocities in the narrow upstream part lead to higher erosion and

lower sedimentation in the river bed and thus a thinner riverbed is assumed. In the wider downstream part on the other hand less erosion and higher sedimentation occurs, leading to a thicker riverbed.

#### 4.1.4 Western Boundary

The western boundary is defined as a Dirichlet constant head boundary. Its shape is defined by the coast of the Chtouka plain along the Atlantic Ocean (Figure 4.2). Head stages at this boundary are assumed to be at a constant sea level of 0 m.a.s.l. over the whole modelling period.

### 4.2 Geological Model

In a previous work, Horn (2021) built a geological model of the Chtouka aquifer (Figure 4.4) on the basis of lithological drilling data from 100 boreholes, geophysical measurements and a geological map of the region. This model is used in this study and shown in Figure 4.4. In the following, its main characteristics will be summarised. For more detailed information refer to the cited study.

Over the modelling area, five different lithological units, each assumed as homogeneous over its spatial extent, were identified. These units are:

- calcareous sediments,
- gravel,
- sand,
- schist and
- silty sand.

Of these, calcareous sediments, sand and schist form the group of main units with large spatial extents.

Schist is considered to be the oldest stratigraphical unit. It outcrops in the eastern part of the aquifer and is covered by sediments towards the west. Above the schist lies in most regions a layer of calcareous marl with a mean thickness of 100 m. Although showing in reality local variations between more sandy and more clayey areas, it is over-all assumed as one lithological unit. Apart from an area in the south where this lithological unit outcrops, calcareous marl is covered by one of the three remaining strata. Predominantly the overlying layer is sand, which also forms the top of the aquifer in most areas. While reaching its estimated maximum thickness of 150 m along the coast, the layer thins towards the eastern part. The north east of the model is characterised by alluvial fans of varying compositions of clay, sand and gravel in both horizontal and vertical direction.

This area is modeled by the two lithological units silty sand and gravel. Each geological unit is defined by its specific material properties, which are the hydraulic conductivities  $K_h$  in horizontal and  $K_v$  in vertical direction (both in  $\text{m s}^{-1}$ ) as well as the corresponding horizontal and vertical anisotropies (–), the porosity  $\phi$  (–), the specific yield  $S_y$  (–) and specific storage  $S_s$  ( $\text{m}^{-1}$ ).

The top of the aquifer corresponds to the topographic surface and is defined by the DEM of NASA JPL (2013), which has a  $30 \text{ m} \times 30 \text{ m}$  resolution. The bottom boundary of the aquifer is defined by Horn (2021) depending on the local stratification of the lithological units. As a basis, unweathered schist is generally assumed to be a confining aquitard at depth. However, schist may become a water bearing stratum due to weathering. Following McFadden et al. (2005) this weathering is considered to reach at most 50 m into the unit. This maximum depth may occur only in regions where the schist crops out, as this is the case in the eastern parts of the model area. Where the schist is overlain by other strata, the weathered depth should accordingly be reduced (Note: This however is not directly stated in Horn (2021), but follows from the fact that in the model schist also appears in regions where it is not the top layer). This leads to a minimum depth of the aquifer of 50 m in relation to the local surface elevation in all regions. In the central area, thicknesses of the aquifer are estimated by the depths of the locally deepest drilled boreholes. In the northern part of the Chtouka aquifer, data from measuring campaigns of vertical electrical soundings in the period 1947 to 2008 in the Souss Massa Basin are used to define the bottom of the aquifer. For the coastal areas, transient electromagnetics measurements (Kalberkamp et al., 2021) from a campaign within the framework of the CREM project are used.

## 4.3 Recharge from Precipitation

Precipitation data were compiled by Horn (2021) and will be briefly described in the following. For more information, refer to the cited study.

For estimations of the local precipitation, datasets from meteorological stations in Agadir, Ait Melloul, Ait Amira, Biougra and at the YBT dam were available. Based on these data three zones were identified, which account for the spatial variations of precipitations due to regional differences in altitude and climate. These zones are shown in Figure 4.2.

The northwestern zone has the highest average annual precipitation of  $220 \text{ mm a}^{-1}$  over the modelling period (1968-2020). The central zone, which incorporates the largest area of the model region, and the southeastern zone are characterised by a significantly lower annual precipitation of  $190 \text{ mm a}^{-1}$  respectively  $160 \text{ mm a}^{-1}$  over the modelling period.

The infiltration rates of the precipitation are estimated basing on the top-most lithological unit and expected evaporation from the ground. Therefrom infiltration rates of 6 %

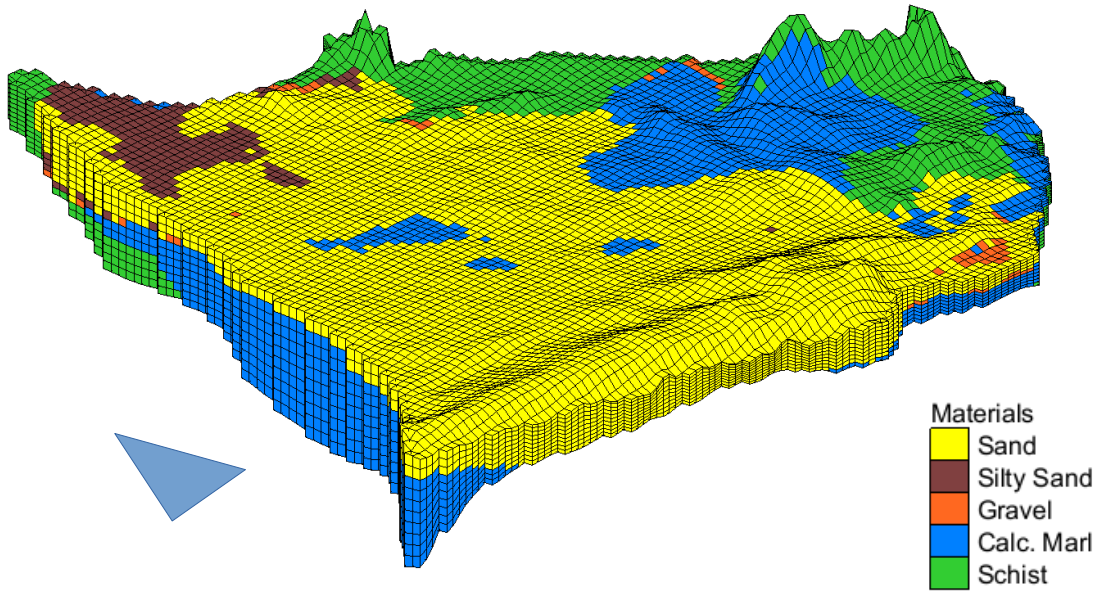


Figure 4.4: The already geological model of the Chtouka aquifer, as defined by Horn, 2021. The  $xy$ -plane is oriented along the four cardinal directions with the positive  $x$ -direction pointing to the north (arrow). In the  $xy$ -plane cell edges have a length of 500 m. For presentation purposes, a  $z$ -magnification with a factor of 10 is applied.

of the precipitation follow for the northern and central areas and 5 % for the southern area (RESING and AQUAPLAN, 2008). The derived annual time series of recharge from precipitation are shown for the three areas in Figure 4.5.

## 4.4 Groundwater Wells

Groundwater extraction through wells has been examined in various studies by the ABHSM. Thus, data are available from different databases. This data has been previously analysed by the project team and processed to fit the modelling needs. In the following, the main features are summarised. For detailed information refer to the technical notes in Appendices A and B in Horn (2021). Each well is characterised by a name, its location in the  $xy$ -plane and its top elevation, the depth to the top of the screen and the screen length as well as by a time series of estimated or measured flow rates. All wells can be distinguished into two classes. The first class encompasses manually dug wells, the second drilled and reconnaissance wells. This classification has been used to interpolate missing data concerning the vertical screen locations and screen lengths of some wells. Furthermore, the wells can be additionally classified through the utilisation of the extracted water, which is either for drinking and domestic purposes or for irriga-

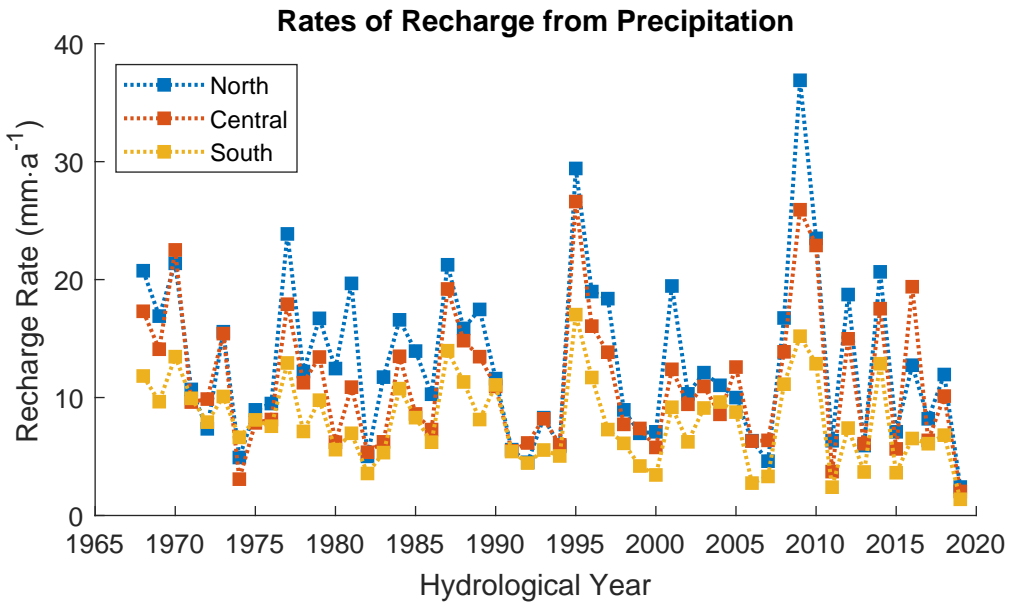


Figure 4.5: Time series of annual groundwater recharge in the three different zones (Figure 4.2) as identified by Horn, 2021.

tion. Based on the end user, pumping rates have been estimated for wells with missing data.

#### 4.4.1 Drinking Wells

A total of 380 wells are considered as drinking wells in the study area. These are depicted in Figure 4.6(a). Data on extracted water volumes are available for the time periods 1969-2001 from one single source and 2001-2020 from several sources. Based on these datasets pumping volumes and therewith pumping rates are estimated for the whole period from 1969 to 2020. Information on commissioning of new wells is only available until 2003. After 2003, the further commissioning of wells is assumed as being coupled to the population growth and is assigned a yearly growth rate of 0.7%, thus slowly increasing the extracted water volume.

#### 4.4.2 Irrigation Wells

Data regarding the irrigation wells is available from two surveys carried out in 2003 and 2015. In the study from 2003, a total of 2448 wells are recorded and in 2015 a number of 3050 wells. Due to significant differences in either location (the vast majority) or in well characteristics (for wells with similar coordinates) both sets of wells are considered as disjunct. Therewith a total of 5498 irrigation wells is considered in this study (Figure

4.6 (b)). Data from the studies are based on personal records or memorizations from farmers and estimates for each well or each farm made during the surveys.

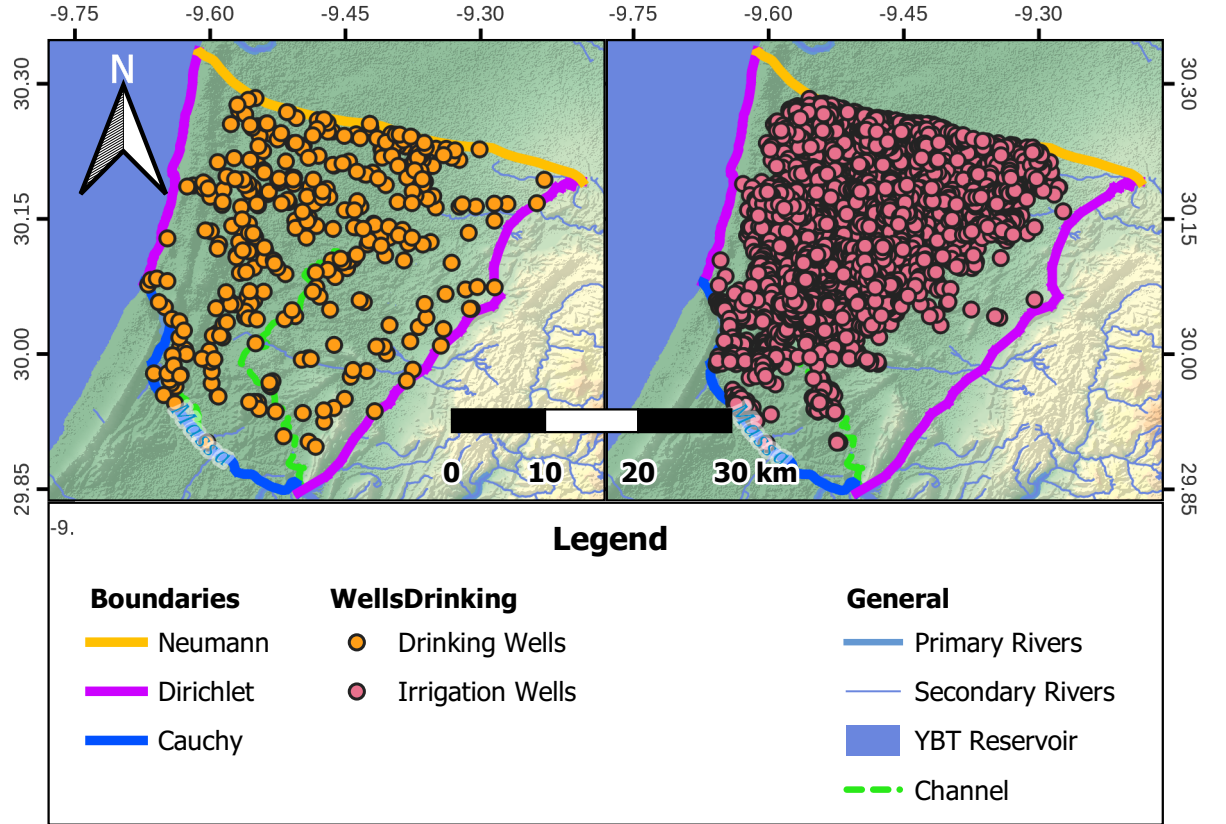


Figure 4.6: Spatial distribution of the in this study considered 5498 irrigation wells (left) and 380 drinking wells (right).

## 4.5 Irrigation Returns

As described in Section 3.5, the Chtouka plain is extensively used for agricultural activities. As stated introductory to this section, a certain portion of the applied irrigation water re-infiltrates into the aquifer and leads to groundwater recharge. To account for this recharge, both the spatial extents and the infiltration rates of the applied water are estimated as described in this section.

The Tassila perimeter already existed in 1968 and its extent has stayed constant since then Bernet and El Habil (1977). The public perimeter exists since the commissioning of the YBT dam in 1974. The extents of both perimeters are assumed as constant. An analysis of satellite pictures from different years shows a significant change over

time for the private perimeter. To account for this evolution, the perimeter's extents are estimated for six consecutive periods (1968-1973, 1974-1979, 1980-1989, 1990-1999, 2000-2009 and 2010-2020).

Within the three perimeters the three different irrigation techniques flooding, sprinkler and drip irrigation are used. Inside each of the three perimeters, a homogeneous spatial distribution of the applied techniques is assumed. Over time, the frequency ratios of the different methods vary as previous studies show (RESING, 2003, ANZAR CONSEIL, 2016). Based on these studies the temporal evolution of the frequency ratios is estimated for each of the three perimeters. Infiltration rates are finally calculated depending on these distributions.

## 4.6 Observations

Observational data of head measurements are available from 27 piezometers that are scattered over the study area (Figure 4.2). These observations cover different time periods within 1968-2020.

At four locations a respective pair of piezometers is available that is covering successive time periods. The second ones were built as, due to the local drawdown of the ground-water table, the originally installed piezometers fell dry. From these piezometers, for each pair a combined, longer time series can be generated. Therewith, observations are available for 23 distinct locations.

Furthermore, the observed head data is calculated from two measurements: A one-time measurement of the  $z$ -location of the top of the piezometer, and a second, continuous measurement of depth from the surface to the watertable. Thus, piezometers can be divided into two main groups, based on the determination of  $z$ : levelling and topography map reading. For levelled piezometers, an error of 1 m is assigned. For non-levelled piezometers, this error is 10 m.



# **Chapter 5**

## **Implementation of the Model**

### **5.1 Implementation of the Model**

#### **5.1.1 Modelling Software: GMS**

In this study the Groundwater Modeling System (GMS) software by Aquaveo, LLC. is used as modelling environment. It is a common software applied in the field of hydraulic, hydrologic and groundwater modelling and is used by many federal and local governmental agencies around the world (Aquaveo, 2021).

Regarding the fundamental flow calculations GMS bases on the modular finite-difference flow model MODFLOW (McDonald and Harbaugh, 1988), which is available in various versions. To simulate seawater intrusion, the three-dimensional multi-species solute transport model MT3DMS (Zheng and Wang, 1999) and the variable-density groundwater flow model SEAWAT (Langevin, 2009) will be applied in future studies to the here examined model. As SEAWAT bases on MODFLOW-2000 (Harbaugh et al., 2000), in this study this particular MODFLOW version is used.

MODFLOW itself is divided into a series of processes and packages. While major tasks are organised as processes, more specific tasks are executed by packages leading to the eponymous modularisation. Therefore, each optional package provides a different functionality. To utilise these particular functionalities, the corresponding packages need to be activated for the single elements of a GMS model.

In GMS numerical groundwater models are generated either by direct manipulations of a defined three-dimensional grid or by a conceptual modelling approach, as it is applied in this study. For this latter approach GMS utilises common GIS-objects such as points, arcs and polygons which are defined as distinct features on different layers. Each layer represents one homogeneous class of objects - one of the above mentioned feature types - which correspond to one specific term of the groundwater flow equation (Section 5.1.2).

### 5.1.2 Model Equations

As a basis for future work, in the scope of this study the temporal evolution of a constant-density flow in the Chtouka aquifer is to be considered. The assumption of constant density implies two simplifications of the real world system: First the incompressibility of the flowing medium water, second the neglect of saltwater intrusion. Therewith the groundwater flow in the system that is schematically depicted in Chapter 4 is described by the groundwater flow equation (2.14),

$$S_s \frac{\partial h}{\partial t} = \frac{\partial}{\partial x} \left( K_{xx} \frac{\partial h}{\partial x} \right) + \frac{\partial}{\partial y} \left( K_{yy} \frac{\partial h}{\partial y} \right) + \frac{\partial}{\partial z} \left( K_{zz} \frac{\partial h}{\partial z} \right) + \dot{M}_{ss,i} \quad (5.16)$$

where  $K_{xx}$ ,  $K_{yy}$  and  $K_{zz}$  denote the hydraulic conductivities in ( $\text{m s}^{-1}$ ) along the  $x$ -,  $y$ - and  $z$ -axis respectively,  $h$  the potentiometric head in (m),  $S_s$  the specific storage of the porous medium ( $\text{m}^{-1}$ ) and  $t$  the time (s).

$\dot{M}_{ss,i}$  denotes the different source- and sink-terms  $i$  as volumetric flux per unit volume ( $\text{s}^{-1}$ ). These are following the conceptual model here the recharge from precipitation, the withdrawal from both drinking and irrigation wells and the irrigation returns. Negative values of  $M_{ss,i}$  imply flow out of the system and positive values flow into the system.

As explained in Section 2.2 only the diagonal elements  $K_{ii}$  of the hydraulic conductivity tensor are here considered. In the deviation of the equation this is possible due to the arbitrary choice of orientation of the coordinate system in the single control volumes parallel to the major axes of the hydraulic conductivity (Harbaugh et al., 2000). However it may be noted that in MODFLOW-2000 only a global coordinate system is considered. As stated in Section 5.1.4 this coordinate system is oriented along the cardinal directions.

### 5.1.3 Implementation of the Conceptual Model in GMS

The in this study used geological model was implemented by Horn (2021) in GMS first as a triangulated irregular network (TIN). It was then discretised as described in Section 5.1.4. The material properties of the geological units that are relevant for this study are the hydraulic conductivities  $K$  and specific storage  $S_s$ , as can be seen from the groundwater flow equation (2.14). In this study the hydraulic conductivities are assumed to be horizontally isotropic,  $K_{xx} = K_{yy}$ , and in vertical direction to have an anisotropy with a factor of 10,  $K_{xx} = 10 \cdot K_{zz}$ . As the geological model represents a simplification of the aquifer, exact values of the named parameters need to be estimated basing on the model's behaviour. This is described in Section 5.2.

The other layers of the in Chapter 4 described conceptual model are imported as distinct layers into GMS. The different features corresponding to each layer are represented by one of the common GIS-objects, as specified in Table 5.1. The different MODFLOW

packages applied to each layer are listed here as well. As GMS can process only non-overlapping polygons in one layer, the over time varying private irrigation perimeters are defined on several layers. Therefore each identified period of constant extents (e.g. 1968-1973, see Section 4.5) is implemented in a single layer, leading to a total of six layers for the private irrigation perimeter. As the public and Tassila perimeters do not overlap, these are assigned to one single, shared layer.

Table 5.1: Overview of the in GMS implemented layers. Each layer is comprised of features of the specified object class and utilises the listed MODFLOW packages.  
(\*) : The time-dependent areas of the private perimeter are divided by corresponding periods into six layers (Section 5.1.1).

Layer	GIS-feature type	utilised packages
Boundary East	arc	LPF, CHD1
Boundary South	arc	LPF, RIV1
Boundary West	arc	LPF, CHD1
Precipitation Areas	polygon	RCH1
Drinking Wells	point	WEL1
Irrigation Wells	point	WEL1
Irrigation Returns Private (6x) <sup>(*)</sup>	polygon	RCH1
Irrigation Returns Public+Tassila	polygon	RCH1
Piezometers	point	Trans. Head

## 5.1.4 Discretisation

The groundwater flow equation (2.14) is a non-linear, inhomogeneous partial differential equation. Therefore it cannot trivially be solved analytically for the described system. Within the framework of GMS the equation is therefore solved numerically. A three-dimensional cartesian grid is generated and Equation (2.14) is solved on this grid for defined time steps using the finite difference method. For further details on the solution method refer to Harbaugh et al. (2000).

### Spatial Discretisation

In this study the by Horn, 2021 derived three-dimensional discretised geological model is used. It bases on an implementation of the original geological model as from which the three dimensional grid was generated using the grid overlay approach in MODFLOW-2000.

In horizontal direction the resulting grid has a quadratic cell size of 500 m × 500 m with cell edges oriented in the four cardinal directions. Positive  $x$ -direction points to the east, positive  $y$ -direction to the north (Figure 4.4). In vertical direction, the model is

set to a thickness of 10 equally spaced layers with therefore in  $x$ - and  $y$ -direction locally varying depths. Positive  $z$ -direction points upwards. The minimum layer thickness is set to 2.5 m. The top- and bottom-most cell faces are defined as variably shaped surfaces, depending on the DEM and the bottom of the solids. The shapes of the inter-cellular faces are linearly interpolated between the outer two. To each cell the lithological unit locally incorporating the largest volume is assigned, defining the cell's material properties.

### Temporal Discretisation

Regarding the temporal discretisation, MODFLOW 2000 utilises a division into stress periods and time steps. Stress periods are generally defined in GMS as periods of constant transient stresses (e.g. pumping rates, precipitation). Each stress period can have a particular length and is further sub-divided into a number of equally long time steps.

For this model stress periods are defined as the single hydrological years, which start on 1st of September at 00:00:00 of one year and end on 31st of August of the subsequent year at 23:59:59. They therewith show a variable length due to leap years. The number of time steps is set to two per stress period. The correctness of this approach was successfully tested through comparison of simulations with otherwise constant parameters, showing equality.

## 5.2 Methodology of Sensitivity Analysis and Calibration

The true behaviour  $T$  of a system can be either measured, through which an experimental value  $E$  is obtained. Or it can be modeled, which yields a modelling value  $M$ . In either case, the results obtained deviate from reality due to measuring errors  $\delta_E$  or modelling errors  $\delta_{SM}$  (Stern et al., 2001),

$$T = E - \delta_E \quad (5.17)$$

$$T = M - \delta_{SM} \quad (5.18)$$

Although models represent a simplified version of reality, they are often described by complex mathematical equations that cannot be solved analytically. Therefore the exact modelling value  $M$  is numerically approximated by a simulation value  $S$ . Likewise, this value underlies a numerical error  $\delta_{SN}$  (Stern et al., 2001),

$$M = S - \delta_{SN} \quad (5.19)$$

The simulation result can be expressed as function  $f$  of system inputs (the key variables)  $\mathbf{X}$  and parameter combinations  $\boldsymbol{\theta}$  (Naeini et al., 2019),

$$S = f(\mathbf{X}, \boldsymbol{\theta}) \quad (5.20)$$

In this study each specific combination  $\boldsymbol{\theta} = (\theta_1, \dots, \theta_N)$  of values  $\theta_i$  of the  $N$  different parameters  $i$  is called a parameter set. All possible parameter sets constitute the parameter space  $\Theta$ .

The adequacy of a model for a specific purpose can be assessed through its capability to describe the behaviour of the real system. Thus with Equations (5.18), (5.19) and (5.20) follows:

$$T = f(\mathbf{X}, \boldsymbol{\theta}) - (\delta_{SM} + \delta_{SN}) \quad (5.21)$$

To achieve a close fit of the model to the reality, it is necessary to minimise the numerical and modelling errors. The prior can be decreased among others through the choice of an adequate discretisation and solution scheme as well as through the refinement of the discretisation. The latter depends on both the modelling function  $f$  itself and the choice of a suitable parameter set  $\boldsymbol{\theta}$ .  $f$  is defined through the modelling equations whose exact formulation depends on the conceptual model. Therefore after assembling a model to a state as far as described for the here applied model, a further reduction of the simulation error is only possible through an adjustment of the model parameter values  $\boldsymbol{\theta}$ .

A model's response significantly depends on these parameters. An example is shown in Figure 5.1. Depending on the choice of the specific parameter set, the modelling error varies. This variation is generally non-linear and can show a great deal of interaction between the different parameters (Duan et al., 1993). Thus within the parameter space  $\Theta$  not only one global optimum may exist for which the modelling error reaches its global minimum ( $\boldsymbol{\theta}_{go}$  corresponding to a point within the green area in Figure 5.1). But there also may be several other local optima at which the modelling error becomes locally minimal. In Figure 5.1 these are within the closed yellow and orange areas in the top-left, of which one is exemplarily marked corresponding to  $\boldsymbol{\theta}_{lo}$ .

The process of finding the parameter set corresponding to the global minimum of  $\delta_{SM}$  is called calibration. The procedure used in this study is described in Section 5.2.3.

As the function  $f(\mathbf{X}, \boldsymbol{\theta})$  is often unknown, calibration needs to be conducted by simple trial-and-error. Therefore it is computationally expensive and if carried out manually also very time-consuming. However, not all model parameters impact the model results equally extensive (Duan et al., 1993). Therefore, the number of parameters considered in calibration of a model can preliminarily be reduced to only those parameters with significant impact. To identify these different impacts, the behaviour of the model to changes in single parameters is examined in a sensitivity analysis prior to the calibration.

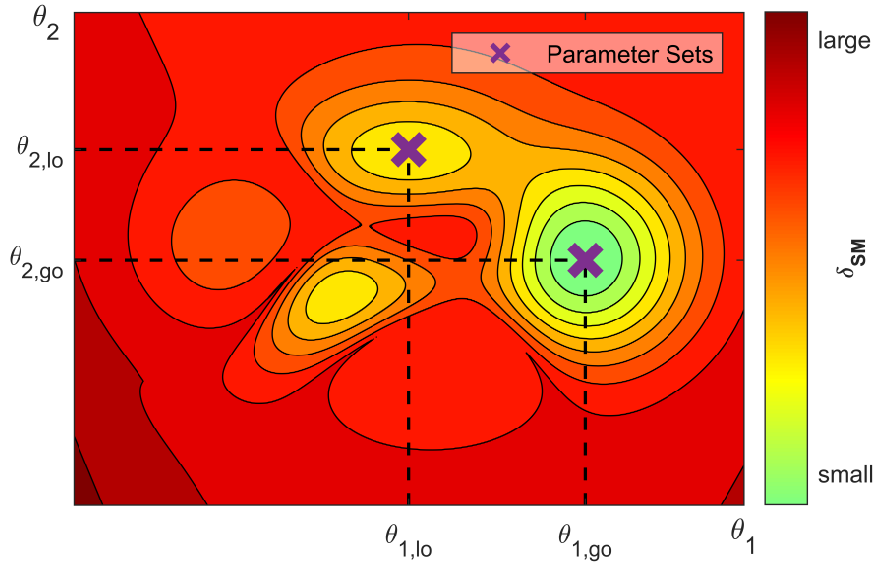


Figure 5.1: Example of a two dimensional continuous parameter space  $\Theta$  with elements  $\boldsymbol{\theta} = (\theta_{1,i}, \theta_{2,j})$ . Each of these parameter sets corresponds to an absolute modelling error  $\delta_{SM}$  marked by the colour scale. In this example, the parameter set  $\boldsymbol{\theta}_{lo}$  corresponds to a local minimum of the modelling error  $\delta_{SM}$ . The global optimum of  $\delta_{SM}$  is obtained by the parameter set  $\boldsymbol{\theta}_{go}$ .

The procedure of the sensitivity analysis that this study follows is described in Section 5.2.2.

Crucial to the success of both sensitivity analysis and calibration is the meaningful measurement of the modelling error  $\delta_{SM}$ . Several different measures exist that have different characteristics. Section 5.2.4 describes the methodology followed in this work.

Prior to sensitivity analysis and calibration however, the examined parameters need to be identified. In this study, not all model parameters are taken into account. Those examined in the sensitivity analysis are described in the following Section 5.2.1.

### 5.2.1 Examined Parameters

In this study, three groups of parameters are identified for which the model is to be calibrated. Two of these directly follow from the groundwater flow equation (2.14): the hydraulic conductivities  $K_{ii}$  and the specific storage  $S_s$ . For the third one it is acknowledged that the estimations of the pumping rates underly a large uncertainty. Therefore the associated sink-term  $\dot{M}_{ss,irr}$  is provided with a scaling factor  $\theta_{Q,irr}$ .

Both the hydraulic conductivities and the specific storages are material properties and characterise the geological model for the flow model. Therefore, both have specific values

for each of the five lithological units into which the model is divided. Although each of the parameters therewith corresponds to a defined unit, exact values are unknown. This is due to the coarse classification into five lithological units of the possibly more heterogeneous geology of the aquifer. Likewise, characterisations in literature differ.

A within the project framework conducted literature research identified for hydraulic conductivities a range of values over several orders for each material. The corresponding minimum and maximum values are listed in Table 5.2.1. Therewith no direct specification between the hydraulic conductivities in  $x$ -,  $y$ - and  $z$ -direction are possible. To reduce the dimensions of the parameter space, certain assumptions are made. First, as the flow directions in the  $xy$ -plane vary in space while no location-dependent variation of  $K_{xx}$  and  $K_{yy}$  is possible within the model framework, a horizontal isotropy is assumed,

$$K_h = K_{xx} = K_{yy} \quad (5.22)$$

where  $K_h$  is the horizontal hydraulic conductivity. Second, a constant anisotropy between horizontal and vertical hydraulic conductivity is assumed with a proportionality factor of 10,

$$K_h = 10 K_v = 10 K_{zz} \quad (5.23)$$

with the vertical hydraulic conductivity  $K_v$ . In the following the hydraulic conductivities will be expressed in terms of the horizontal hydraulic conductivities  $K_h^{(i)}$  of the materials  $i$ .

In the same, prior to this study conducted literature research it was found that few values for the specific storage are available in literature. Therefore, more data concerning the specific yield and the effective porosity of probes is given. Thus, the values for the specific storage are approximated with Equation (2.7) through the specific yield  $S_y$  and the aquifer thickness  $b$ . Values for the specific yield can either be measured directly or approximated as equalling the effective porosity of a probe. The identified range of values for these two quantities are shown in Table 5.2.1. The aquifer thicknesses  $b$  refer to average thicknesses of the respective lithological units. However, these thicknesses are not constant but vary significantly in space. To account for this the geological model is examined statistically. From this analysis ranges of the material thicknesses are estimated. The corresponding limits are defined by the 20 %- and 80 %-Quantiles (Table 5.2.1). From these estimations of  $S_y$  and  $b$  the ranges of values for the material-specific specific storages are calculated as described. The results are shown in Table 5.2.1. In the following the specific storages will be expressed as  $S_s^{(i)}$  of the materials  $i$ .

Regarding the uncertainties of the pumping rates of the irrigation wells, prior to this study an expert on plant hydrology was consulted. An assessment was done on how realistic the yearly withdrawn water volumes might be. The estimations base on the expectable evapotranspiration when taking into account the irrigated area and cultivated

Table 5.2: Overview of the value ranges of the parameters horizontal hydraulic conductivity  $K_h$  and specific storage  $S_s$  for all materials. Furthermore the value ranges of specific yield  $S_y$  and material thickness  $b$  are listed that were used to calculate the specific storages.

Material	$K_h$ ( $\text{m s}^{-1}$ )		$S_y$ (-)		$b$ (m)		$S_s$ ( $\text{m}^{-1}$ )	
Calc. Marl	$1 \cdot 10^{-6}$	$1 \cdot 10^{-4}$	23	38	21	109	$2 \cdot 10^{-3}$	$2 \cdot 10^{-2}$
Gravel	$1 \cdot 10^{-7}$	$9 \cdot 10^{-5}$	2	10	20	85	$2 \cdot 10^{-4}$	$4 \cdot 10^{-3}$
Sand	$8 \cdot 10^{-5}$	$1 \cdot 10^{-2}$	17	24	13	54	$3 \cdot 10^{-3}$	$2 \cdot 10^{-2}$
Silty Sand	$1 \cdot 10^{-7}$	$1 \cdot 10^{-3}$	10	40	32	350	$3 \cdot 10^{-4}$	$1 \cdot 10^{-2}$
Gravel	$4 \cdot 10^{-7}$	$5 \cdot 10^{-4}$	1	26	23	140	$7 \cdot 10^{-5}$	$1 \cdot 10^{-2}$

plant species. As result, an underestimation of water withdrawal volumes by a factor of 2 was deemed possible. Thus, the range of values for the scaling factor of the irrigation flow rate is set to an interval of

$$\theta_{Q,irr} = [0.5, 2.0] \quad (5.24)$$

In total, a parameter set  $\boldsymbol{\theta}$  therewith comprises of five values of hydraulic conductivities, five values of specific storages and one value of the scaling factor  $\theta_{Q,irr}$  of the irrigation flow rate. The parameter space is accordingly 11-dimensional.

## 5.2.2 Methodology of the Sensitivity Analysis

For the sensitivity analysis a basic parameter set  $\boldsymbol{\theta}_3$  is picked as reference. To examine the model's behaviour in respect to the different parameters, each parameter is varied separately in respect to this parameter set within its defined ranges. The model's behaviour to changes of this single parameter within the defined parameter set is assumed as being representative also for other parameter sets. Therefore the underlying parameter set is chosen to represent average values of the parameters and not extreme values. Thus,  $\boldsymbol{\theta}_3$  is defined as the geometric averages of the different parameters. In this study, the model's response  $S$  is evaluated for five values of each parameter.

The hydraulic conductivities and specific storages from Table 5.2.1 often range over several orders. Therefore a logarithmic partition of the defined intervals is applied with constant proportionalities between neighbouring values. Accordingly, the middle value  $\theta_{i,3}$  of parameter  $i$  denotes the geometrical average. The set of the five examined values  $\theta_{i,1}, \dots, \theta_{i,5}$  is defined by

$$\bigcup_{j=1, \dots, n} \theta_{i,j} : \theta_{i,j} = \left( \frac{\text{Max}(\Theta^{(i)})}{\text{Min}(\Theta^{(i)})} \right)^{\frac{j-1}{n-1}} \cdot \text{Min}(\Theta^{(i)}) \quad (5.25)$$

where  $n$  is the number of values, thus  $n = 5$ . The response  $S$  of the model is measured through analysis of the dependent variable head  $h$ , as described in Section 5.2.4.

### 5.2.3 Methodology of the Calibration

The goal of the calibration is to identify a parameter set  $\boldsymbol{\theta}$  that globally minimises the modelling error  $\delta_{SM}$ . However, as described before also local minima of  $\delta_{SM}$  may exist, and therewith several major areas to which a search strategy may converge within the feasible parameter space as described by Duan et al. (1993). Within these areas possibly numerous local optima both close to and at various distances from the best solution may be localised. Furthermore, the parameters can show a great deal of - possibly non-linear - interaction and compensation (Duan et al., 1993). Thus, the start of a search strategy requires a large enough number of points to identify major areas of attraction. Within these areas a succeeding clustering focussed on the most promising regions is recommended. However, the clustering should not be limited to a small area to sustain robustness of the search against local optima (Duan et al., 1993).

In this work, the calibration is conducted manually, including both the changing of the parameter values on each simulation run and the corresponding evaluation of the model's results. In the following, the algorithm used as orientation is described. However, deviations from the strict pattern appear. This is since during the original calibration process the ranges of the single parameters were adjusted, for various reasons.

As the calibration is conducted solely manually in this study, a parallel multi-dimensional clustering is not feasible. Therefore a sequential approach is applied, that is divided into a number of steps  $k$ . Each such step is comprised of a cycle over the different parameters. Within each such cycle, the parameters are optimised successively with a single iteration. Therefore, for each iteration an interval  $[\theta_{i,k,min}, \theta_{i,k,max}]$  for parameter  $i$  is defined. On this interval,  $n = 5$  or  $n = 7$  values are calculated in analogy to Equation (5.25) by

$$\bigcup_{j=1,\dots,n} \theta_{i,k,j} : \theta_{i,k,j} = \left( \frac{\theta_{i,k,max}}{\theta_{i,k,min}} \right)^{\frac{j-1}{n-1}} \cdot \theta_{i,k,min} \quad (5.26)$$

The interval boundaries  $\theta_{i,k,min}$  and  $\theta_{i,k,max}$  are defined as the nearest neighbours  $\theta_{i,k-1,j-1}$  and  $\theta_{i,k-1,j+1}$  of the optimal value  $\theta_{i,k-1,j}$  from the previous step  $k-1$ . If  $j = 1$  or  $j = n$ ,  $Min(\Theta^{(i)})$  or  $Max(\Theta^{(i)})$  is used as respective lower or upper interval limit. From these parameter values, the one with the smallest corresponding error  $\delta_{SM}$  is chosen. Through this approach it is tried to avoid a too focussed clustering while maintaining a sufficient reduction of interval limits over each iteration, and thus keeping a balance between computational costs, robustness and accuracy. Calibration is stopped when either the simulation output shows throughout one step only small variations or the limits of the parameter space are reached.

### 5.2.4 Error Assessment

Common measures for error estimation are the root mean square error (*RMSE*) and the mean absolute error (*MAE*). These average single errors  $y_i - \hat{y}_i$  between a measurement value  $y_i$  and a reference value  $\hat{y}_i$  over all  $n$  instances  $i$  through different averaging methods. *RMSE* and *MAE* are defined by

$$RMSE = \sqrt{\sum_{i=1}^n \frac{(y_i - \hat{y}_i)^2}{n}} \quad (5.27)$$

$$MAE = \frac{\sum_{i=1}^n |y_i - \hat{y}_i|}{n} \quad (5.28)$$

The mean absolute error therewith represents the arithmetic average of the single errors  $y_i - \hat{y}_i$ , thus giving each error the same weight on a linear scale. The *RMSE* on the other hand, as it first squares the single errors, weights larger errors higher than smaller errors.

In the previous study by Horn (2021), the error of the model was estimated through these two measures. Therefore the spatially distributed measuring points were regarded as an ensemble. Thus the underlying 3-dimensional continuous scale holding the spatial information could be reduced to a 1-dimensional nominal scale, with the identifier being the piezometer name. Therewith an average response of the model - where the aquifer is regarded as a unit - to changes in parameter values could be estimated. In this study however, the model is regarded in transient state. This introduces an additional dimension, the time. This dimension's scale, as it is discrete and not nominal, holds information about correlations between the values. Trivially, values at later times depend on values at preceding times. Using one of the aforementioned error measures thus leads to loss of information about these dependencies, since every point in time is regarded as an independent instance. This issue is illustrated in Figure 5.2 (a): All three simulations have the same *RMSE* in comparison to the observation time series, but their temporal evolution deviates significantly from each other. Simulation 1 shows no time dependent behaviour at all. In case of Simulation 2 the long-term trend matches that of the observation. However, the results underlie an offset in head. In case of Simulation 3 the initial offset is even larger, but diminishes until the end of the measuring period due to an underestimation of the long-term trend. An error analysis using the *RMSE* could not distinguish between these different cases. However, depending on the application the different behaviours may be suitable in different ways. Therefore, the *RMSE* and the *MAE* - for analogue reasons - are deemed unfit for the assessment of time series data as in this study.

To derive a more adequate measuring method the correlation between the observed dependent variable and the simulated dependent variable are considered. In Figure 5.2

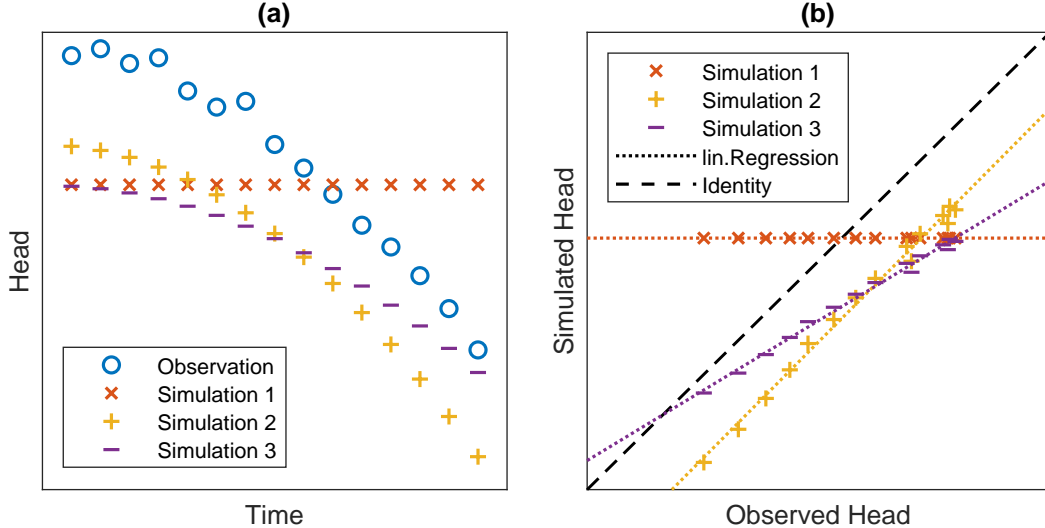


Figure 5.2: (a): Time series of an observation and of three simulations with different parameter sets. In comparison with the observation all three simulations have an equal  $RMSE$ . (b): Linear representation of the correlations between observed and simulated heads for the three simulations from (a). The respective data sets are each fitted with a linear (lin.) regression. The black dashed line marks identity between observed and simulated head.

this is illustrated for the here used dependent variable head  $h$ . As basis, it is assumed that a correlation between these two exists and that it can be approximated as linear relationship. Therewith it can be parametrised through linear regression,

$$S \approx p_0 + p_1 E \quad (5.29)$$

with the regression coefficients  $p_0$  and  $p_1$ . The therewith defined linear curves are also depicted in Figure 5.2.

Graphically,  $p_1$  denotes the slope of the curve. For determination of the coefficients, least-squares fitting is applied in this study. Therewith, values in proximity to the limits affect the choice of  $p_1$  with a higher weight, as in these regions the residuals are more sensitive to the coefficient. Under the assumption that short-term fluctuations of hydraulic head in an aquifer are of significantly smaller amplitude than long-term trends, this coefficient is primarily affected by the latter. Thus,  $p_1$  can be understood as comparing the long-term trends of simulation  $S$  and observation  $E$  with each other. Values  $p_1 \approx 1$  denote a similar representation of the trends from the observations by the simulation. Values  $p_1 > 1$  or  $0 < p_1 < 1$  indicate an overestimation or an underestimation of the observed trend, respectively. Values  $p_1 < 0$  denote an under- or overestimation of the trend, but in opposite direction - e.g. while in the observed time series a drawdown of hydraulic head exists, the simulation results would give an increase in hydraulic head.

To estimate long-term trends from observational data, observations need to cover sufficiently long time periods. In this study, only time series covering 7 or more years are considered for estimation of  $p_1$ . Furthermore, as at four locations a respective pair of piezometers is covering separate time periods (Section 4.6), their time series are merged pairwise. To account for the higher certainty at these locations, each piezometer is in the evaluation still considered a single independent observation point, but with the merged time series. This gives each of the piezometer pairs a doubled weight in respect to the other piezometers.

$p_0$  denotes the intercept of the fitted curve with the  $y$ -axis of the correlation plot. In this application it marks therewith the simulation value that would occur for an observation value  $E = 0$ . Such a value however may not be reached in the described, real system, and thus  $p_0$  is a primarily mathematical quantity. Furthermore,  $p_0$  highly depends on the interval of simulation values and empirical values that are compared. For intervals over large observation values of exclusively the same sign, small changes in  $p_1$  result in significant changes of  $p_0$ . Also, each measuring location may have an individual observation error  $\delta_E$ . For the aforementioned issues however, this error cannot directly be incorporated into  $p_0$ . To overcome these issues, a standardisation in respect to the actual values of  $S$  and  $E$  is necessary. As in this study time series are regarded, the initial offset

$$\Delta S_0 = T(t=0) - S(t=0) \quad (5.30)$$

is chosen as representation of the true parallel shift between the truth  $T$  and the simulation  $S$  at time  $t=0$ . However, in this study only 8 out of 27 available observation time series date back to the here chosen initial date, the year 1968. To still allow the assessment of the other time series in respect to this characteristic, values are extrapolated for  $T(t=0)$  in the affected cases. Therefore the assumption is made that the modeled trends sufficiently correlate to the observed trends. To obtain an expression for  $T(t=0)$ , Equation (5.29) can first be written for  $t=0$  as

$$S(t=0) = p_0 + p_1 \cdot E(t=0) \quad (5.31)$$

Solving for  $E(t=0)$  yields

$$E(t=0) = \frac{S(t=0) - p_0}{p_1}$$

Together with Equation (5.17), Equation (5.2.4) can thus be written as

$$\Delta S_0 = \frac{S(t=0) - p_0}{p_1} - \delta_E - S(t=0)$$

rewriting finally yields

$$\Delta S_0 = S(t=0) \cdot \left( \frac{1}{p_1} - 1 \right) - \frac{p_0}{p_1} - \delta_E \quad (5.32)$$

As  $\Delta S_0$  depends on  $1/p_1$ , it may be noted that  $\Delta S_0$  is only defined for values  $p \neq 0$ .

In real systems, numerous processes occur that influence its behaviour in different extents. A model does not account for all these processes. Furthermore measurements of dependent variables, that are also modeled underlie measuring errors  $\delta_E$ . Together, this leads to fluctuations in the measurement value  $E$  that are not reproduced by a model. Likewise, inaccurate modelling of single processes can lead to fluctuations of the simulation value  $S$  in respect to  $E$  (which is strictly speaking equivalent the former and in formulation only a matter of perspective). Such fluctuation highly influence the accuracy of the here applied error measurement approach, as it bases on the assumption of some linear correlation between observation and simulation result. To which extent a model is able to reproduce the variation of the observations through simulation results, and whether it adds more fluctuation than is actually present in the observational data can be estimated by the coefficient of determination,  $R^2$  (Mosteller and Tukey, 1977). It is defined by

$$R^2 = \left( \frac{n \sum (S \cdot E) - (\sum S)(\sum E)}{\sqrt{[n \sum S^2 - (\sum S)^2] \cdot [n \sum E^2 - (\sum E)^2]}} \right)^2 \quad (5.33)$$

with  $n$  denoting the number of elements of the respective time series. As can be seen from the definition,  $R^2$  is symmetrical and can therefore be understood as how much of the variation of  $E$  can be explained by  $S$ , and vice versa. Its values range between 0 and 1, with values close to 0 indicating weak linear correlation between variations, and 1 indicating high linear correlation.



# Chapter 6

## Results and Discussion

### 6.1 Sensitivity Analysis

The results of the sensitivity analysis are shown in Figures 6.1-6.9 for each of the three parameter groups hydraulic conductivity  $K_h$ , specific storage  $S_s$  and scaling factor of the irrigation well pumping rates  $\theta_{Q,irr}$  and each of the error measures initial offset  $\Delta S_0$ , slope coefficient  $p_1$  and coefficient of determination  $R^2$ . Here, boxplots are chosen for representation. Each parameter set-specific box comprises of the  $n$  instances of values, one for each qualified piezometer. As described in Section 5.2.4, for  $\Delta S_0$  and  $p_1$  piezometers are excluded with time series shorter than 6 years. Furthermore,  $p_1$  a logarithmic scale is naturally appropriate. In favour of recognisability, in this presentation of the results additional graphs for negative values are omitted. Thus, and to preserve consistency and comparability, piezometers showing at any global instance negative values of  $p_1$  are excluded in graphs of  $p_1$ . For calculation of  $\Delta S_0$  however, this does not apply. Therewith, the following analysis bases on 20 piezometers for  $p_1$  and 25 piezometers for  $\Delta S_0$  and  $R^2$ , out of a total of 27 piezometers. For each graph, the medians (+) are marked, along with the arithmetic averages in case of  $\Delta S_0$  and  $R^2$  or the geometric averages in case of  $p_1$  ( $\times$ ). Generally, for the different parameters the model shows different sensitivities.

In case of the hydraulic conductivity of schist, the model does not converge for the smaller values  $\theta_{Schist,1}$  and  $\theta_{Schist,2}$ , thus their respective boxplots are missing in the respective graphs. Regarding the initial offset  $\Delta S_0$  (Figure 6.1), sand, gravel, calcareous marl and schist show significant changes on the boxplots, medians and arithmetic averages. For silty sand, only a small variation for larger values can be observed. Regarding the impacts on  $p_1$  (Figure 6.2) only comparably small variations or none at all can be observed for sand, silty sand and gravel. Slightly larger variations occur for schist and calcareous marl. For smaller values of  $K_h$ , changes in the boxplots and the arithmetic averages can be observed for sand and calcareous marl, while the respective medians show no variation. This indicates that not all piezometers are affected equally from changes in the parameter values. Finally, for  $R^2$  (Figure 6.3) significant changes can only be observed for calcareous marl and schist and when regarding the boxplots. Both medians and means show no significant changes, indicating that only single piezometers

are affected. This can also be seen when regarding the outliers, that for higher values of  $K_h$  become slightly larger and thus are statistically treated as within the wedges.

For the specific storage  $S_s$ , the model converges for all examined parameter variations in respect to the reference parameter set. For  $\Delta S_0$  (Figure 6.4), all boxplots show only little variation compared to  $K_h$ . While gravel and calcareous marl seem to not have any impact on the simulation values, significant non-monotonic variations especially of the arithmetic average can be observed for the other three materials. The comparably large impact on the arithmetic mean can here again be explained by variations of single piezometers. Nonetheless, variations also occur for the respective medians, indicating shifts in the whole subset of piezometers. In comparison to the horizontal hydraulic conductivity (Figure 6.2) the specific storage has a significantly larger impact on the slope coefficient  $p_1$  (Figure 6.5). For calcareous marl and gravel only some outliers are slightly affected. For sand boxplots, means and medians show significant changes. For schist and silty sand these variations are even higher, for schist with an approximate factor of 5 over the full range. On  $R^2$  (Figure 6.6), the specific storage also has for all materials only small impacts in average. For sand and schist, single piezometers however appear to be affected significantly.

Finally, the scaling factor of the irrigation pumping rates  $\theta_{Q,irr}$  shows on both initial offset  $\Delta S_0$  (Figure 6.7) and  $p_1$  (Figure 6.8) very large impacts. For  $\Delta S_0$  non-monotonic behaviour can be observed, whereas for  $p_1$  monotonic behaviour occurs. Once again,  $R^2$  (Figure 6.9) is affected only for single piezometers.

All in all, the different sensitivities are summarised in Table 6.1. It can be seen, that in average  $K_h$  has a significantly larger impact on  $\Delta S_0$  and  $S_s$  has a significantly larger impact on  $p_1$ . This goes in line with the fact that commonly  $K_h$  is calibrated for the initial steady state and  $S_s$  for the transient state. Nonetheless, smaller impacts appear also on the respective other error measure. This indicates that it might be reasonable to calibrate these two parameters following an alternating scheme as described in Section 5.2.3.

Without knowledge of the effect on the single piezometer, information about the can be drawn from the here portrayed boxplots. Therefore, a depiction of the excessively many 27 piezometer-specific time series can here and for the further analysis be omitted. It can be seen that the parameters have different impacts over the modelling area. For the material-specific parameters this is to be expected, as the lithological units are not homogeneously distributed. Regarding the scaling factor for pumping rates of irrigation wells  $\theta_{Q,irr}$ , an analogue statement is reasonable.

For both parameter groups it can furthermore be stated that not all materials have similar impacts on the simulation results. In case of the hydraulic conductivity, silty sand appears to be rather negligible. The same applies for calcareous marl and gravel when regarding the specific storage  $S_s$ . The scaling factor  $\theta_{Q,irr}$  has a significant impact on both parameters. For  $p_1$  this is not surprising, as groundwater withdrawal in the Chtouka aquifer increases over time and an overexploitation of the aquifer is observed.

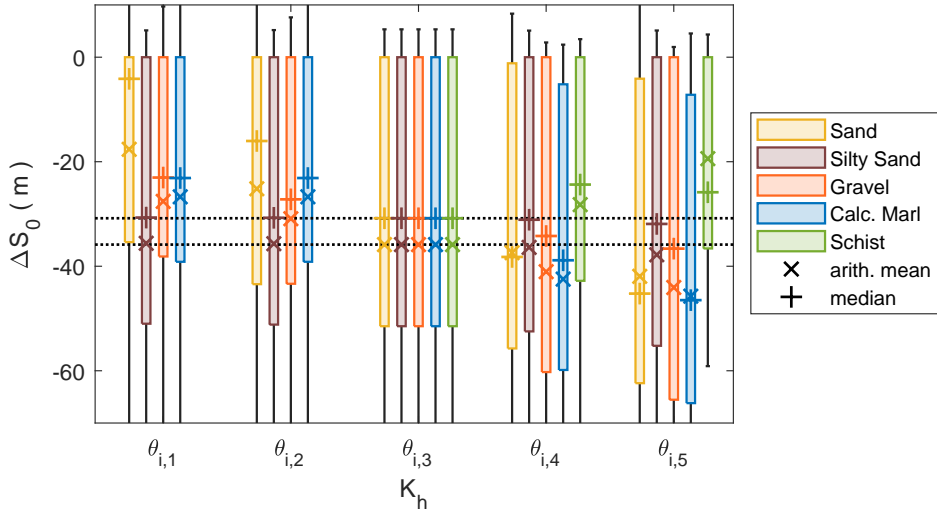


Figure 6.1: Sensitivity of the model towards the parameter  $K_h$  for all five materials  $i$ , measured by the error  $\Delta S_0$ . The corresponding parameter values  $\theta_{i,j}$  are defined by Equation (5.25) and thus increase from left to right on a logarithmic scale. Each boxplot comprises the same set of piezometers. Whiskers and outliers are cut off for better perceptability. The black dotted lines mark the medians (+) and arithmetic means  $\times$  of the reference parameter  $\theta_{i,3}$ .

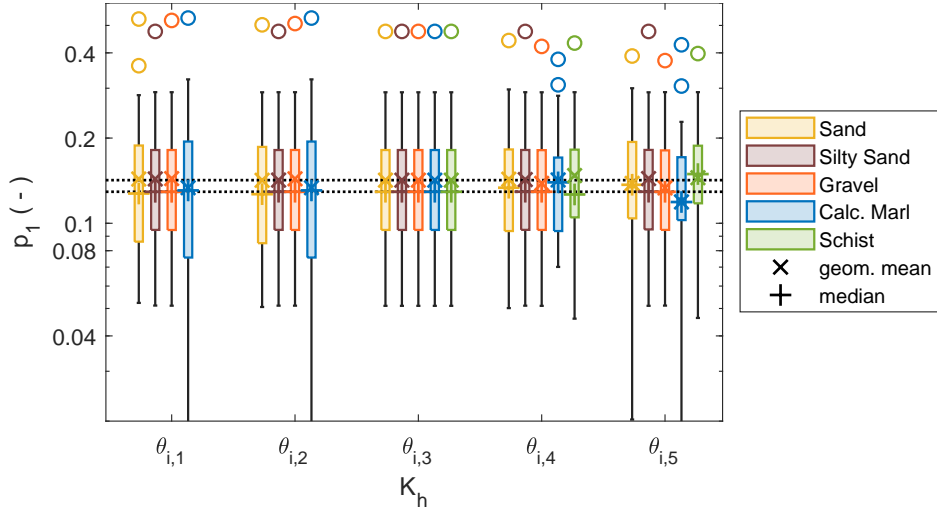


Figure 6.2: Sensitivity of the model towards the parameter  $K_h$  for all five materials  $i$ , measured by the error  $p_1$ . The corresponding parameter values  $\theta_{i,j}$  are defined by Equation (5.25) and thus increase from left to right on a logarithmic scale. Each boxplot comprises the same set of piezometers. Whiskers and outliers are cut off for better perceptability. The black dotted lines mark the medians (+) and arithmetic means  $\times$  of the reference parameter  $\theta_{i,3}$ .

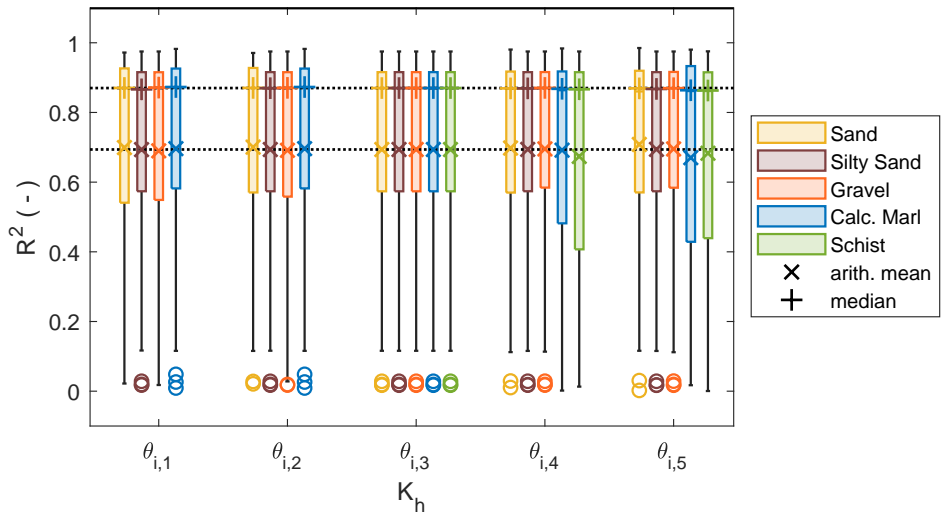


Figure 6.3: Sensitivity of the model towards the parameter  $K_h$  for all five materials  $i$ , measured by the error  $R^2$ . The corresponding parameter values  $\theta_{i,j}$  are defined by Equation (5.25) and thus increase from left to right on a logarithmic scale. Each boxplot comprises the same set of piezometers. Whiskers and outliers are cut off for better perceptability. The black dotted lines mark the medians (+) and arithmetic means  $\times$  of the reference parameter  $\theta_{i,3}$ .

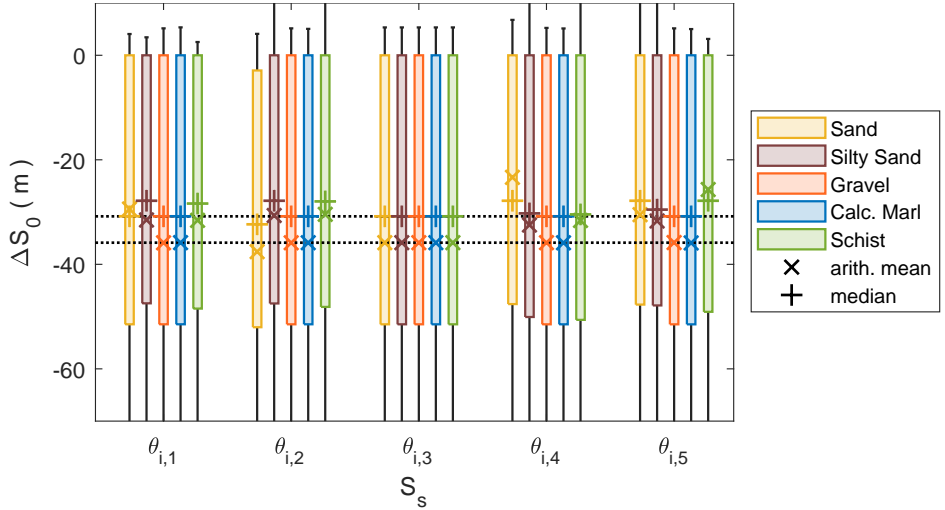


Figure 6.4: Sensitivity of the model towards the parameter  $S_s$  for all five materials  $i$ , measured by the error  $\Delta S_0$ . The corresponding parameter values  $\theta_{i,j}$  are defined by Equation (5.25) and thus increase from left to right on a logarithmic scale. Each boxplot comprises the same set of piezometers. Whiskers and outliers are cut off for better perceptability. The black dotted lines mark the medians (+) and arithmetic means  $\times$  of the reference parameter  $\theta_{i,3}$ .

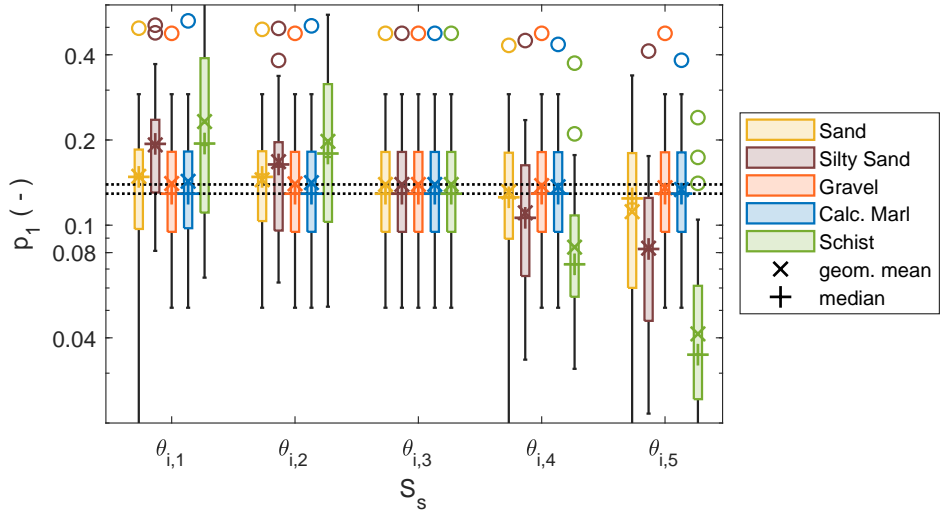


Figure 6.5: Sensitivity of the model towards the parameter  $S_s$  for all five materials  $i$ , measured by the error  $p_1$ . The corresponding parameter values  $\theta_{i,j}$  are defined by Equation (5.25) and thus increase from left to right on a logarithmic scale. Each boxplot comprises the same set of piezometers. Whiskers and outliers are cut off for better perceptability. The black dotted lines mark the medians (+) and arithmetic means  $\times$  of the reference parameter  $\theta_{i,3}$ .

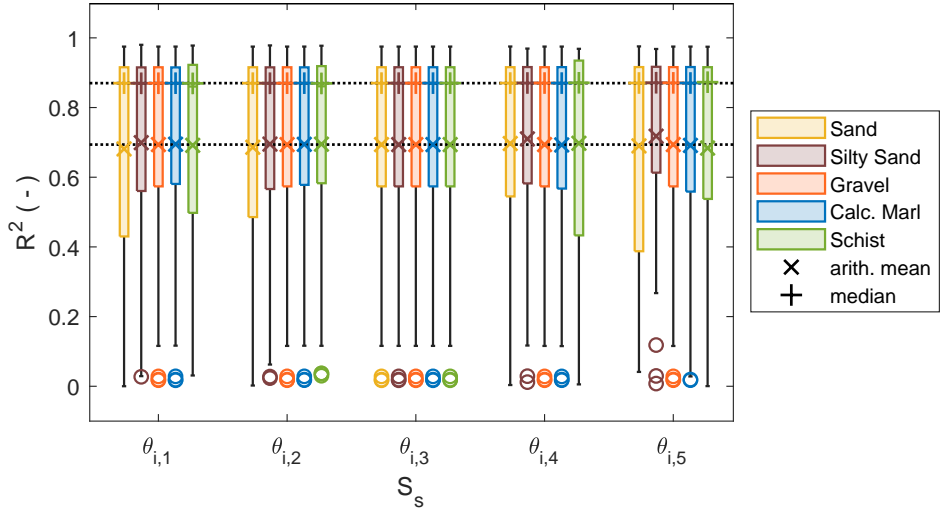


Figure 6.6: Sensitivity of the model towards the parameter  $K_h$  for all five materials  $i$ , measured by the error  $R^2$ . The corresponding parameter values  $\theta_{i,j}$  are defined by Equation (5.25) and thus increase from left to right on a logarithmic scale. Each boxplot comprises the same set of piezometers. Whiskers and outliers are cut off for better perceptability. The black dotted lines mark the medians (+) and arithmetic means  $\times$  of the reference parameter  $\theta_{i,3}$ .

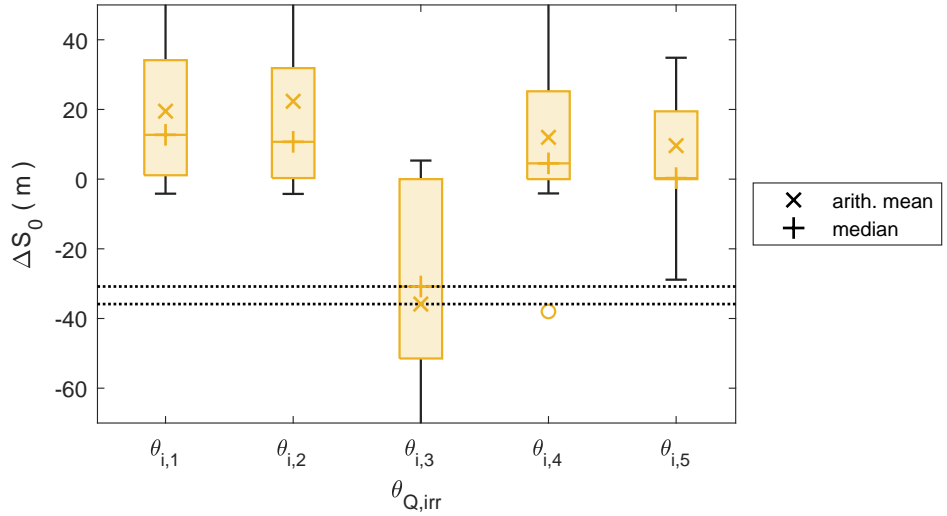


Figure 6.7: Sensitivity of the model towards the parameter  $\theta_{Q,irr}$ , measured by the error  $\Delta S_0$ . The corresponding parameter values  $\theta_{i,j}$  are defined by Equation (5.25) and thus increase from left to right on a logarithmic scale. Each boxplot comprises the same set of piezometers. Whiskers and outliers are cut off for better perceptability. The black dotted lines mark the medians (+) and arithmetic means  $\times$  of the reference parameter  $\theta_{i,3}$ .

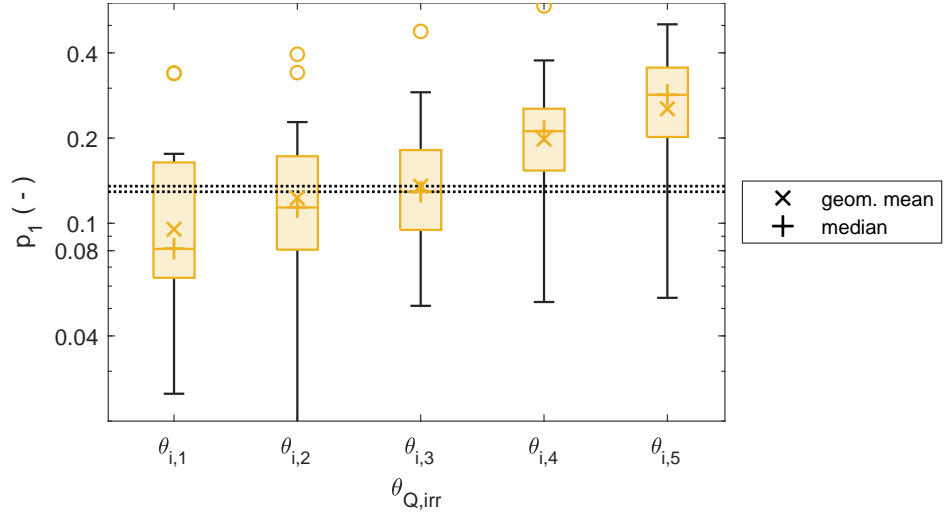


Figure 6.8: Sensitivity of the model towards the parameter  $\theta_{Q,irr}$ , measured by the error  $p_1$ . The corresponding parameter values  $\theta_{i,j}$  are defined by Equation (5.25) and thus increase from left to right on a logarithmic scale. Each boxplot comprises the same set of piezometers. Whiskers and outliers are cut off for better perceptability. The black dotted lines mark the medians (+) and arithmetic means  $\times$  of the reference parameter  $\theta_{i,3}$ .

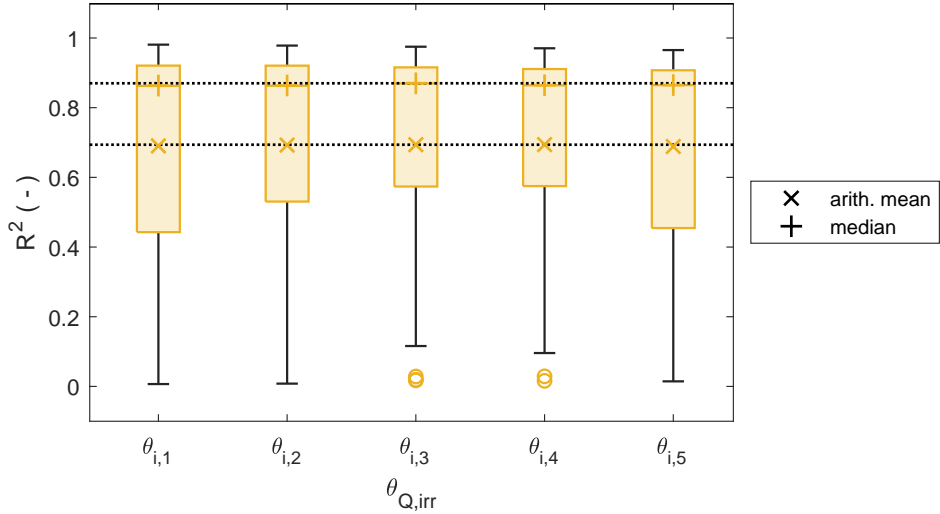


Figure 6.9: Sensitivity of the model towards the parameter  $\theta_{Q,irr}$ , measured by the error  $R^2$ . The corresponding parameter values  $\theta_{i,j}$  are defined by Equation (5.25) and thus increase from left to right on a logarithmic scale. Each boxplot comprises the same set of piezometers. Whiskers and outliers are cut off for better perceptability. The black dotted lines mark the medians (+) and arithmetic means  $\times$  of the reference parameter  $\theta_{i,3}$ .

For  $\Delta S_0$  however, this is unexpected as for the initial time in 1968 only little groundwater extraction takes place. Therewith, the impact on the simulation results at this time should be small. A possible explanation for this however is that  $\Delta S_0$  gives an inaccurate estimation for the targeted quantity. This in turn can be caused by a too inaccurate estimation of the underlying trend, also indicated by  $R^2$ .  $R^2$  itself shows only little sensitivity for all parameters. This is reasonable, since the different parameters do not introduce new processes into the model depending on the parameter values, but rather scale the corresponding processes. Significant impacts on averages of  $R^2$  are therewith only expectable, if the choice of parameter values is so extreme that they induce a relative binary behaviour. This means that for example a parameter value becomes so small that the underlying process is effectively inactivated in respect to others, or so big that it becomes extremely dominant. This however is a rather theoretical concept, as for a model such values probably lead to convergence errors (confer  $K_h^{(Schist)}$ ).

Finally, basing on the previous discussions the number of parameters relevant for the model calibration can be reduced by 3:  $K_h^{(SiltySand)}$ ,  $S_s^{(Calc.Marl)}$  and  $S_s^{(Gravel)}$ . Therewith the dimensions of the parameter space for calibration becomes 8.

Table 6.1: Summary of the sensitivities of the different error measures  $p_1$ ,  $\Delta S_0$  and  $R^2$  to the material-specific parameters  $K_h$  and  $S_s$  and the other parameter  $\theta_{Q,irr}$ . Sensitivities are measured on the following ordinal scale: ++: highly sensitive, +: sensitive, o/+: sensitive in only single parameters, averages and medians not significantly affected, o: not significantly sensitive.

Material	$K_h$			$S_s$			$\theta_{Q,irr}$		
	$p_1$	$\Delta S_0$	$R^2$	$p_1$	$\Delta S_0$	$R^2$	$p_1$	$\Delta S_0$	$R^2$
Calc. Marl	+	++	o/+	o	o	o	++	++	o
Gravel	o	++	o	o	o	o			
Sand	+	++	o	++	+	o/+			
Schist	+	++	o/+	++	+	o/+			
Silty Sand	o	o/+	o	++	+	o/+			

## 6.2 Calibration

The calibration is conducted according to Section 5.2.3. In total, 310 simulations are conducted over 7 iteration steps. Figure 6.10 shows the results during the calibration process, displayed through the respective arithmetic ( $\Delta S_0$ ) and geometric ( $p_1$ ) averages. For comparison, the arithmetic mean of the  $RMSE$  is plotted as well (Section 6.3). Of the in total 7 iteration steps the last one yields results that are varying only slightly. Depicted are the simulation results of the respectively picked parameter sets. The first six iteration steps are shown aggregated, while the last is shown in its entirety. The partly large variations (especially at the end of iteration 5) stem from adjustments to the parameter ranges. This also causes the large jump between  $K_h^{(Calc.Mar)} and  $K_h^{(Sand)}$ . In the end of the calibration, four different values of  $\theta_{Q,irr}$  are compared: factors of 1.0, 1.3, 1.5 and 1.7. As can be seen, this parameter highly impacts the final result. As final parameter set,  $\theta_{Q,irr} = 1.3$  is taken, since it represents the supposedly most reasonable trade-off between acknowledged uncertainty of  $M_{irr}$  and a good result of the calibrated model. This is important, as for the real application time proceeds. Therewith, measuring and estimation techniques of the pumping rates are further developed and thus vary, leading to a time-dependence of this factor. For the other calibrated parameters this issue however does not arise, since these represent material properties of the lithological units and can therefore be assumed as constant over time. The final parameter set is listed in Table 6.2.$

## 6.3 Discussion of Error Measures

In Figure 6.10 the  $RMSE$  is also displayed for comparison. Along with the calibration decisions, the  $RMSE$  shows from the first iteration on a monotonic decline in value. Only for the final variation of  $\theta_{Q,irr}$  an partwise increase can be observed. This one

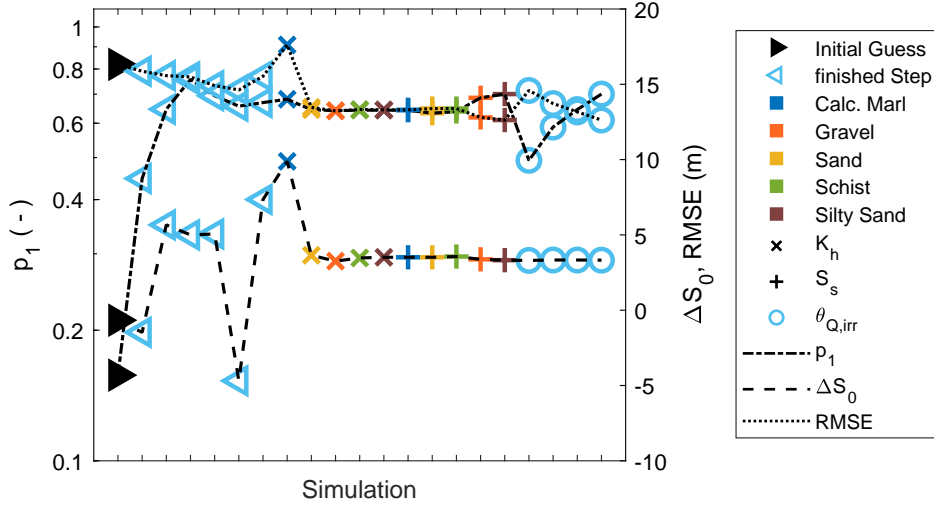


Figure 6.10: The results of the calibration process for the error measures  $p_1$  and  $\Delta S_0$ . The  $RMSE$  is plotted for comparison. Along the  $x$ -axis advances the calibration process, starting on the left with the initial simulation results. All seven executed iterations are depicted. Of these, the first six are shown aggregated as final iteration result. For the last iteration, for each of the material parameters the best-fitting result is shown. The last four instances mark final variations of  $\theta_{Q,irr}$ .

Table 6.2: The values of final parameter set.

Material	$K_h$ ( m )	$S_s$ m $^{-1}$	$\theta_{Q,irr}$ ( - )
Sand	0.00003	0.002	1.3
Silty Sand	0.000009	0.0002	
Gravel	0.005	0.003	
Calc. Marl	0.0004	0.0005	
Schist	0.000006	0.0003	

however is analogue to the behaviour of  $p_1$ . Obviously, the  $RMSE$  seems to lead to analogue calibration decisions. However it may here be noted, that in the regarded graph only one out of five to seven options is depicted. Therefore, it is not possible to determine, if a better fit could have been found along the way. Nonetheless, based on this perception, the  $RMSE$  seems equally fit for calibration as  $\Delta S_0$  and  $p_1$  - or vice versa. However, the here examined calibrating process belongs to a particular model with seemingly only little interactions between the different parameters. For other usecases, especially when parameters significantly impact two of the error measures at a time, they might unfold a higher potential.

Furthermore it can be stated that the initial implementation of the error measures is more laborious. For the experienced programmer however, this may not be a significant impact. Also, the more complex computations require more resources. For most applic-

ations, the computational costs of the simulations might still be significantly higher.

The underlying assumption of this method is that simulation values  $S$  and observations  $E$  show a large enough correlation. This should be a reasonable assumption, as a model is designed to correlate to observations. Additionally, with  $R^2$  a factor for the assessment of this assumption in a particular case is given.

## 6.4 Discussion Lumping of Irrigation Wells

In the current model a total of 5498 wells are included, each as a single point with a corresponding time series. As this amount of data was assumed to cost an extensive portion of computational resources, the possibility of lumping of the groundwater wells should be examined. As the spatial extents of the areas in which groundwater pumping occurs vary over time, this would require several layers of different shapefiles as for the irrigation zones. The loading of the original 5498 pointwise timeseries however proves to take approximately 5 minutes, everytime that changes are made to the underlying data. In case of a lumped representation, each layer would have to be imported separately by hand. This procedure however takes more than the automatic point-wise reading. Therefore the approach is deemed unfavourable and is thus not further examined in this study.

# Chapter 7

## Conclusion

In this study, the steady state model by Horn (2021) could successfully be expanded to a transient constant-density flow model. On this, future work can further advance by generalising it to a variable density model. Therewith, possible scenarios of management decisions and environmental influences can be examined on their impacts on the system, to facilitate sustainable development of the water resources in the region.

Although there are no direct indications that through the derived parameters a significantly different result could be obtained than under application of the *RMSE*, the examined error measures may show greater impacts in calibration processes of other models where a larger interaction between different parameters exists and single parameters may influence several different characteristics of a model.

As the final results show, there might be an inaccuracy of  $\Delta S_0$ . This however has not yet been examined further in this study. For future applications it is therefore of interest, if the interpreted meaning of  $\Delta S_0$  holds against reality. To test this with the here examined data, time series dating back to the initial date 1968 are valuable. With these a testing might be possible. Therefore a randomised process can be used, which generates - not necessarily disjunct - subsets of consecutive years time series with varying lengths. The estimates of  $\Delta S_0$  can for these then be compared to the actual initial offsets. Through repeated executions of the randomised process, an average error of  $\Delta S_0$  can be determined. However, it is to be noted with this method that only a small number of specific cases is considered, which could be inapt for the testing.



# Bibliography

- Agence du Bassin Hydraulique de Souss Massa (2022a). *Eau Souterraine: Evaluation des eaux*. Webpage. Accessed: 17.09.2022. URL: [www.abhsm.ma](http://www.abhsm.ma).
- (2022b). *Etat de remplissage des retenues de barrages 07/09/2022 à 08h00*. Webpage. Accessed: 13.09.2022. Agence du Bassin Hydraulique de Souss Massa. URL: [www.abhsm.ma](http://www.abhsm.ma).
- (2022c). *Situation Hydrologique*. Webpage. Accessed: 20.09.2022. URL: [www.abhsm.ma/index.php/partenariat-5/situation-hydrologique](http://www.abhsm.ma/index.php/partenariat-5/situation-hydrologique).
- ANZAR CONSEIL (2016). *Etude et élaboration de contrat de nappe de Chtouka - BdD "Prélèvements Nappe Chtouka"*. Tech. rep. No public access, information as cited in provided project data.
- Aquaveo, LLC. (2019). *GMS:Conductance*. Accessed: 13.09.2022. URL: [www.xmswiki.com/wiki/GMS:Conductance](http://www.xmswiki.com/wiki/GMS:Conductance).
- (2021). *Aquaveo Webpage*. Accessed: 06.09.2022. URL: [www.aquaveo.com/](http://www.aquaveo.com/).
- Bernet, G. (1968). *Care hydrogéologique de la plaine des Chtouka*. Piezometric map.
- Bernet, G. and A. El Hebil (1977). “Plaine de Chtouka”. In: *Ressources en Eau du Maroc, Tome 3: domaine atlasique et sud-atlasique*. Notes et Mémoires du Service Géologique du Maroc 231, pp. 202–211.
- Choubert, G. (1964). *Histoire géologique du Précambrien de l'Anti-Atlas*. 162. Éditions du Service géologique du Maroc.
- Choukr-Allah, R., A. Nghira, A. Hirich and L. Bouchaou (2017). “Water Resources Master Plan for Sustainable Development of the Souss-Massa River Basin”. In: *The Souss-Massa River Basin, Morocco*. Ed. by R. Choukr-Allah, R. Ragab, L. Bouchaou and D. Barceló. Springer.
- Critchfield, H. (1983). *General Climatology*. 4th ed., p. 453.
- Direction Régionale de Souss Massa (2020). *Annuaire Statistique Régional Souss Massa - 2020*. Tech. rep. Accessed: 18.09.2022. Haut-Commissariat au Plan. URL: [www.hcp.ma/region-agadir/](http://www.hcp.ma/region-agadir/).
- Duan, Q., V. K. Gupta and S. Sorooshian (1993). “Shuffled complex evolution approach for effective and efficient global minimization”. In: *Journal of optimization theory and applications* 76.3, pp. 501–521.
- English, M. (1990). “Deficit irrigation. I: Analytical framework”. In: *Journal of irrigation and drainage engineering* 116.3, pp. 399–412.
- Fetter, C. W. (2001). *Applied Hydrogeology*. 4th ed. Pearson Education International.
- Harbaugh, A. W., E. R. Banta, M. C. Hill and M. G. McDonald (2000). *MODFLOW-2000, The U.S. Geological Survey modular Ground-Water Model - User Guide to*

- Modularization Concepts and the Ground-Water Flow Process.* Tech. rep. U.S. Geological Survey.
- Horn, F. (2021). "Numerical Modelling of Seawater Intrusion in the Chtouka Aquifer, Morocco". MA thesis. Institute of Applied Geosciences, Karlsruhe Institute of Technology.
- Hssaisoune, M., S. Boutaleb, M. Benssaou, B. Bouakkaz and L. Bouchaou (2017). "Physical Geography, Geology, and Water Resource Availability of the Souss-Massa River Basin". In: *The Souss-Massa River Basin, Morocco*. Ed. by R. Choukr-Allah, R. Ragab, L. Bouchaou and D. Barceló. Springer.
- Johnson, A. I. (1967). *Specific yield: compilation of specific yields for various materials*. 1662. US Government Printing Office.
- Kalberkamp, U., M. Tauchnitz and K. Brauch (2021). *Final Report - TEM Measurements in the Chtouka Plain*.
- Krimissa, S., J.-L. Michelot, L. Bouchaou, J. Mudry and Y. Hsissou (2004). "Sur l'origine par altération du substratum schisteux de la minéralisation chlorurée des eaux d'une nappe côtière sous climat semi-aride (Chtouka-Massa, Maroc)". In: *Comptes Rendus Geoscience* 336.15, pp. 1363–1369.
- Langevin, C. D. (2009). *SEAWAT: A computer program for simulation of variable-density groundwater flow and multi-species solute and heat transport*. Tech. rep. U.S. Geological Survey.
- Malki, M., L. Bouchaou, A. Hirich, Y. A. Brahim and R. Choukr-Allah (2017). "Impact of agricultural practices on groundwater quality in intensive irrigated area of Chtouka-Massa, Morocco". In: *Science of the Total Environment* 574, pp. 760–770.
- Matsuura, K. and C. J. Willmott (2018a). *Terrestrial Air Temperature: 1900-2017 Gridded Monthly Time Series (Version 5.01)*. Accessed 16.09.2022. Department of Geography, University of Newark. URL: [http://climate.geog.udel.edu/~climate/html\\_pages/download.html#T2017](http://climate.geog.udel.edu/~climate/html_pages/download.html#T2017).
- (2018b). *Terrestrial Precipitation: 1900-2017 Gridded Monthly Time Series (Version 5.01)*. Accessed 16.09.2022. Department of Geography, University of Newark. URL: [http://climate.geog.udel.edu/~climate/html\\_pages/download.html#T2017](http://climate.geog.udel.edu/~climate/html_pages/download.html#T2017).
- Mays, L. W. and D. K. Todd (2005). *Groundwater hydrology*. 3rd ed. John Wiley and Sons, Inc., Arizona State University,
- McDonald, M. G. and A. W. Harbaugh (1988). *A modular three-dimensional finite-difference ground-water flow model*. U.S. Geological Survey.
- McFadden, L., M. Eppes, A. Gillespie and B. Hallet (2005). "Physical weathering in arid landscapes due to diurnal variation in the direction of solar heating". In: *Geological Society of America Bulletin* 117.1-2, pp. 161–173.
- Ministère de l'Agriculture, de la Pêche Maritime, du Développement Rural et des Eaux et Forêts (2021). *Le Plan Maroc Vert, Bilan et Impacts*. Tech. rep.
- Mosteller, F. and J. W. Tukey (1977). "Data analysis and regression. A second course in statistics". In: *Addison-Wesley series in behavioral science: quantitative methods*.
- Naeini, M. R., B. Analui, H. V. Gupta, Q. Duan and S. Sorooshian (2019). "Three decades of the Shuffled Complex Evolution (SCE-UA) optimization algorithm: Review and applications". In: *Scientia Iranica* 26.4, pp. 2015–2031.

- NASA Jet Propulsion Laboratory (2013). *NASA Shuttle Radar Topography Mission (SRTM) 1 Arc-Second Global*. Accessed 07.09.2022 through USGS, 2018. NASA EOSDIS Land Processes DAAC. doi: /10.5066/F7PR7TFT.
- El-Rawy, M., W. Zijl, A. Salem, A. Awad, M. Eltarably and A. Negm (Sept. 2022). “Fundamentals of Groundwater Modeling Methods and a Focused Review on the Groundwater Models of the Nile Valley Aquifer”. In: pp. 39–70. doi: 10.1007/978-3-031-12676-5\_3.
- RESING (2003). *Etude de la stratégie de gestion des ressources en eau dans le bassin du Souss Massa - Mission 1: Diagnostic de la situation actuelle de la gestion et de l'usage des ressources en eau*. Tech. rep. No public access, information as cited in provided project data.
- RESING and AQUAPLAN (2008). *Plan directeur d'aménagement intégré des ressources en eau (PDAIRE) des bassins Souss Massa*. Tech. rep. No public access, information as cited in provided project data.
- Schütze, N., S. Kloss, F. Lennartz, A. Al Bakri and G. H. Schmitz (2012). “Optimal planning and operation of irrigation systems under water resource constraints in Oman considering climatic uncertainty”. In: *Environmental Earth Sciences* 65.5, pp. 1511–1521.
- Stern, F., R. V. Wilson, H. W. Coleman and E. G. Paterson (2001). “Comprehensive approach to verification and validation of CFD simulations—part 1: methodology and procedures”. In: *J. Fluids Eng.* 123.4, pp. 793–802.
- Taiz, L., E. Zeiger, I. M. Møller, A. Murphy et al. (2015). *Plant physiology and development*. Ed. 6. Sinauer Associates Incorporated.
- Todd, D. K. and L. W. Mays (2005). *Groundwater hydrology*. 3rd ed. John Wiley & Sons.
- U.S. Geological Survey (2018). *Earth Explorer*. Accessed 07.09.2022. Earth Resources Observation and Science (EROS) Center, USGS. URL: <https://earthexplorer.usgs.gov/>.
- Zheng, C. and P. P. Wang (1999). “MT3DMS: a modular three-dimensional multispecies transport model for simulation of advection, dispersion, and chemical reactions of contaminants in groundwater systems; documentation and user's guide”. In.



# **Appendix A**

## **Task of the Master Thesis**

## Masterarbeit

### Numerical investigation of transient water flow in the Chtouka Aquifer, Morocco

Betreuer: Dr. Nelly Montcoudiol (BGR); [nelly.montcoudiol@bgr.de](mailto:nelly.montcoudiol@bgr.de)

Erstprüfer: Prof. Dr. Thomas GRAF (ISU); [graf@hydromech.uni-hannover.de](mailto:graf@hydromech.uni-hannover.de)

Zweitprüfer: NN

**Background** Seawater intrusion is a worldwide phenomenon naturally occurring in coastal aquifers due to the density difference between seawater and freshwater. However, groundwater pumping can induce a landward movement of the freshwater-saltwater interface, which may lead to an increased salinity of the pumped water. In Morocco, the Chtouka region is a major producer of fruits and vegetables intended for exportation. This is only possible through irrigated agriculture and a combined use of surface water and groundwater resources. Intense pumping in the Chtouka aquifer is responsible for the observed water table decline, which exacerbates seawater intrusion and threatens freshwater resources. A recent geophysical survey detected seawater intrusion up to 2.5 kilometers inland. In the near future, water demand is expected to increase due to population growth, increased demand for irrigation and climate change. Consequently, seawater intrusion may move further inland. To investigate the behavior of the seawater intrusion in the Chtouka aquifer, a numerical model was developed using the SEAWAT code (within the GMS software). This model builds on previous existing models and incorporates newly acquired data. As of now, the model has only been calibrated under steady state conditions.

**Objectives** In this project, water fluxes shall be simulated numerically under transient conditions. The transient model includes pumping rates in the area, irrigation return flow, and rainfall. The numerical code SEAWAT (with the GMS software) will be used. In particular, the following aims shall be accomplished:

1. Literature review of the current state of knowledge in this field.
2. Build a transient variable-density 3D flow model for the time 1969-2020. Also build a constant-density flow model without seawater intrusion.
  - 2.1. Impose transient BC (pumping, rainfall, irrigation from recharge).
  - 2.2. Evaluate the impact of the choice of flux along the Eastern Neumann boundary.

- 2.3. Evaluate the impact of the choice of the Southern BC (Cauchy vs. Dirichlet).
  - 2.4. Develop a strategy to quantify existing pumping rates in extraction wells. Verify if groundwater wells can be lumped or need to be imposed point-wise.
  - 2.5. Calibrate the constant-density flow model with existing head measurements.
3. Compare the variable-density flow model with the constant-density flow model.
    - 3.1. Verify the impact of seawater intrusion on the water levels near the coast: Is the variable-density (or constant-density) model adequately reproducing the water level variations in the piezometers near the coast?
    - 3.2. Verify if the results from the variable-density flow model are in agreement with the observed data from subsurface monitoring devices (SMD) and geophysics surveys (TEM).
    - 3.3. Adjust the calibration of the variable-density flow model accordingly

The following additional aims are also anticipated:

4. Generate scenarios (of climatic change and of future water use) in collaboration with the ABHSM, the local partner. Which scenarios to be co-developed will depend on ABHSM interests and data availability.
5. Evaluate their impact on the availability of freshwater resources in the future (water fluxes, seawater intrusion).